Oblique rifting at Tempe Fossae, Mars

Carlos Fernández[1] and Francisco Anguita[2]

Received 8 January 2007; revised 23 March 2007; accepted 22 May 2007; published 25 September 2007.

[1] This work shows the results of a structural study of the faults observed at the Tempe Rift (northeastern Tharsis region), Mars. A new, detailed map of faults and fault systems was used to geometrically characterize the fracture architecture of the Tempe Rift and to measure fault length, displacement, and spacing data, to analyze the spatial distribution of fault centroids, and to investigate the fractal nature of fault trace maps. A comparison with analog models and the use of conventional techniques of fault population analysis show that the Tempe Rift was most probably generated under sinistral oblique-rifting processes, which highlights the importance of the presence of inherited fractures in the tectonic evolution of the Noachian crust. The angle between the extension direction and the rift axis varies along the Tempe Rift, ranging from 50°–60° at its central southern part to 66°–88° to the southwest. Fault scaling relationships are similar to those found at mid-ocean ridges on Earth with exponential fault length-frequency distributions. Localized, inhomogeneous deformation generated weakly interacting faults, spanning the entire thickness of the mechanical layer. This thickness decreased from southwest to northeast along the rift, along with distance from the central part of the Tharsis dome.

Citation: Fernández, C., and F. Anguita (2007), Oblique rifting at Tempe Fossae, Mars, *J. Geophys. Res.*, *112*, E09007, doi:10.1029/2007JE002889.

1. Introduction

[2] From the pioneer works of *Carr* [1974], *Wise et al.* [1979], and *Melosh* [1980], tectonic structures on the Tharsis dome have been extensively studied. Some highlights of this intense scrutiny are the identification of several episodes of tectonism [*Plescia and Saunders*, 1982], the publishing of Tharsis paleotectonic maps [*Scott and Dohm*, 1990], the mapping of stress fields [*Tanaka et al.*, 1991], the hypothesis of nonhydrostatical stresses to account for the contractive deformation [*Watters*, 1993], countered by *Banerdt and Golombek* [2000], who attributed the deformation to flexure alone, the tentative reconstruction of tectonic stages by *Anderson et al.* [2001], and the in-depth regional studies of *Hauber and Kronberg* [2001] at Tempe Fossae, *Cailleau et al.* [2003] at Alba Patera, *Wilkins and Schultz* [2003] at Valles Marineris, or *Borraccini et al.* [2005] at Ceraunius Fossae.

[3] Scarce evidence for strike-slip faulting on Mars has been found to date [e.g., *Ferrill et al.*, 2004]. As exceptions to this point of view we could cite *Forsythe and Zimbelman* [1988], and *Schultz* [1989], who respectively defined strike-slip fault systems at two Tharsis areas, at 5°N 145°W and 23°S 55°W. *Anguita et al.* [2001] characterized another fifteen sets of transcurrent structures, which they dated as Late Noachian-Early Hesperian, and whose origin they suggested to be the result of a period of lithosphere mobility. Similarly, a number of studies (e.g., those of *Watters* [1991, 1993], *Watters and Maxwell* [1983, 1986], *Schultz and Tanaka* [1994], *Anderson et al.* [1999], *Mangold et al.* [2000], and *Mueller and Golombek* [2004]) dealt with the clearly compressional wrinkle ridges. Recently, *Anguita et al.* [2006] have studied the Thaumasia Plateau, the high area south of Valles Marineris, which they propose to be a lithospheric unit thrusted southward. This tectonic transport would explain a number of important transcurrent and thrusting structures, including some rhomb-horst alignments indicative of local transpressional tectonics. On the other side, *Borraccini et al.* [2005] concluded that a significant horizontal crustal motion was needed to explain Ceraunius Fossae, a set of graben near the Tharsis center. The contrast between "load" and "thrust" hypotheses has been increasing as the investigations on Tharsis' structure accumulated. In this context, to define a set of fractures of regional importance as purely extensional or implying a component of strike-slip displacement is surely important when selecting models for the tectonic evolution of the Martian western hemisphere.

[4] The aim of this work is to put forward a detailed examination of fault systems in Tempe Fossae, north of the Tharsis dome. Many previous structural studies dealt with the characteristics and structural evolution of faults in this interesting zone [e.g., *Anderson et al.*, 2001; *Hauber and Kronberg*, 2001; *Wilkins et al.*, 2002]. However, our analysis focuses on one particular faulting episode (described as Tempe Rift by *Hauber and Kronberg* [1999]), and gives an exhaustive description of the fault geometry and scaling properties of this fracturing episode. In the following, we will try to prove that the Tempe Rift is a fine Martian analog

[1]Departamento de Geodinámica y Paleontología, Universidad de Huelva, Huelva, Spain.
[2]Departamento de Petrología y Geoquímica, Universidad Complutense de Madrid, Madrid, Spain.

0148-0227/07/2007JE002889

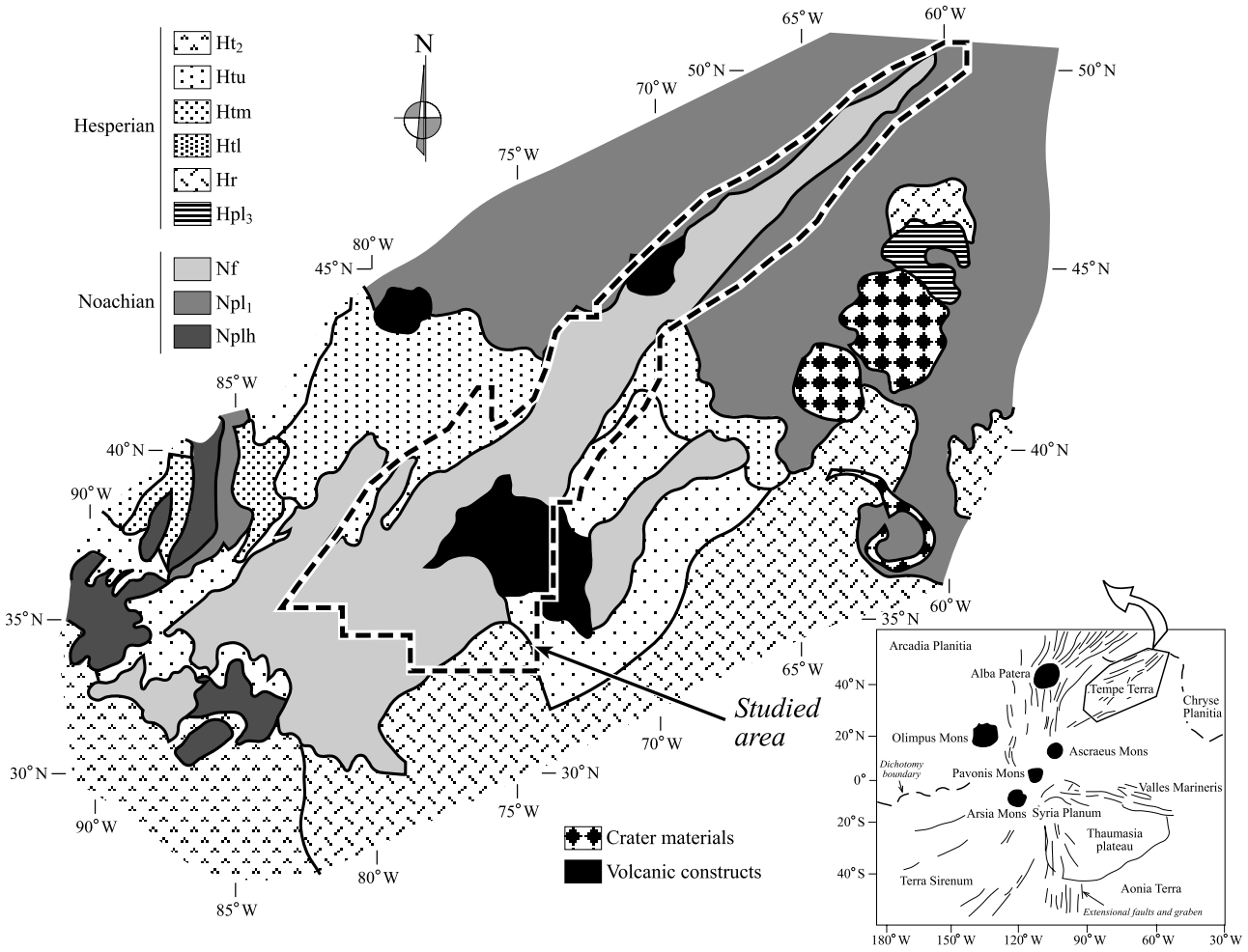

Figure 1. Geological sketch of part of the Tempe Fossae region, including the area studied in this work (modified from *Scott and Tanaka* [1986]). Plateau and high-plains assemblage formed by units Nplh, Hilly unit; Npl_1, Cratered unit; Nf, Older fractured material; Hpl_3, Smooth unit; Hr, Younger ridged plains material; and Htl, Htm, and Htu, lower, middle, and upper Tempe Terra formation, respectively. Western volcanic assemblage represented by Ht_2, Tharsis Montes formation, second unit. Mercator projection. Inset: regional setting of the Tempe Fossae region with respect to Tharsis.

for an oblique rifting structure, in which case the whole fault set would be partly transcurrent, instead of simply extensional. This solution is also supported by the analysis of one of the set of faults performed by *Anguita et al.* [2001] at Labeatis Fossae (30°N 75°W), a shorter (700 km) and nearby (~200 km) fault set which is parallel to Tempe Fossae and shows clear evidence of strike-slip movement. Our detailed study has allowed us to show for the first time the oblique nature of the rifting process in Tempe, a case rarely described on planets apart from Earth. Clearly, an evaluation of the relative importance of strike-slip components of faulting in the kinematics of the Martian lithosphere is necessary before a coherent model of Mars global tectonics could emerge.

2. Geological Setting

[5] Tempe Fossae is a set of faults 2,000 km long located at Tharsis northeastern sector. The structures are mostly mapped as "Older Fractured Material (Nf)" by *Scott and Tanaka* [1986], and are embayed by the Hesperian stratigraphic units Htm ("Tempe Terra Formation, Middle Member"), Htu ("Tempe Terra Formation, Upper Member"), Ht_2 ("Member 2 of Tharsis Montes Formation"), Hr ("Ridged Plains Material"); and V (volcanics of unknown relative age), among others (Figures 1 and 2).

[6] Tempe Fossae has been the subject of several previous works: *Watters and Janes* [1995] suggested that the curved outline of its southern sector (Figure 2) was due to the presence of a corona similar to the Venusian ones. *Hauber and Kronberg* [1999] distinguished four faulting stages affecting the Tempe Fossae region, of which the fourth and most recent stage (the Tempe Rift) corresponds to that studied in our work. *Hauber and Kronberg* [2001] concluded that the similarities in size, amount of extension, and volcanic activity (which they related to a mantle plume) of the Tempe Rift were similar to those of the Kenya Rift; and, on the basis of specific crater counting, they proposed for the structures a minimum age of 3.5 Gy. This agrees with the Noachian age assigned by *Anderson et al.* [2001] to

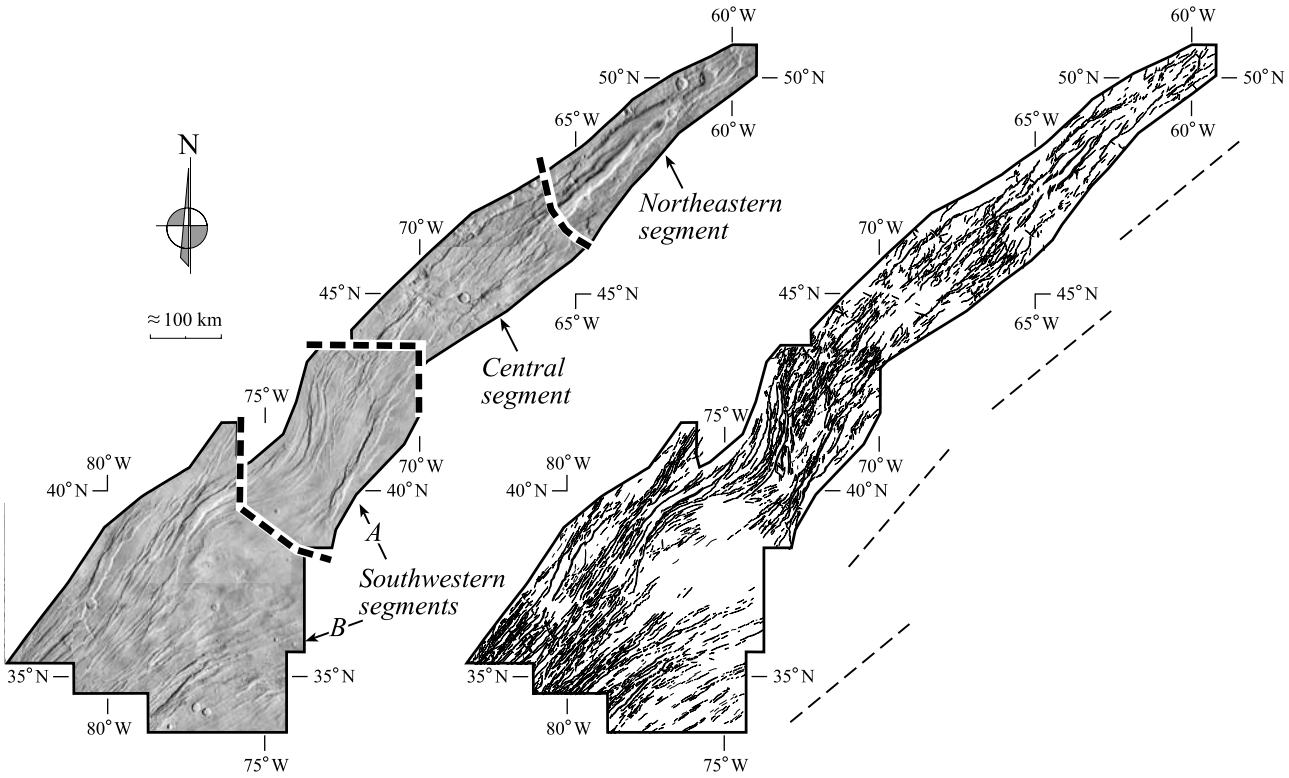

Figure 2. (left) Mosaic of Viking context images of the studied area (Tempe Rift). The mosaic consists of the following Viking Mosaicked Digital Image Models: mi50n070.img, mi50n063.img, mi50n056.img, mi45n072.img, mi45n067.img, mi45n062.img, mi40n082.img, mi40n077.img, mi40n072.img, mi35n082.img, mi35n077.img, and mi35n072.img. Average resolution: 231 m pixel^{-1}. Lines subdividing the Tempe Rift in the four distinct studied segments are marked. (right) Fracture map of the studied area. Faults are not distinguished according to their dip direction. Scale bar valid for the center of both images. Mercator projection.

the same structures. In the most recent investigation of Tempe Fossae, *Wilkins et al.* [2002] hypothesized on the contrary that the distinct fault sets of Tempe Terra have been active from Noachian through Amazonian times, though with a much slower deformation rate than terrestrial rifts. Nevertheless, *Wilkins et al.* [2002] considered the Tempe Rift fault system as Noachian. All investigations agree on the pure extensional character of the structure as a whole, an assumption that will be discussed in this work.

[7] The most exhaustive geometrical analysis of Tempe Rift is that of *Hauber and Kronberg* [2001]. The Tempe Rift structure shows a roughly triangular shape, elongate in an average N45°–50°E trend (Figures 1 and 2). The rift width varies between less than 60 km at its NE vertex to more than 300 km at its SW end. *Hauber and Kronberg* [2001] described with some detail the internal complex pattern of graben and horsts, the geometry of sinuous and en échelon fault traces, fault terraces and rift basins, the location of master faults and rotated blocks, the presence of distinct volcanic edifices related to the structural evolution of the rift, and the regional and local topography according to MOLA data. They also discussed the influence of the preexisting fault patterns on the rift architecture and provided an estimation of the strain and amount of crustal extension associated with the rifting process. *Hauber and Kronberg* [2001] estimated strain values of 3.5–6.7% for the northeastern part of Tempe Rift, with apparently smaller values for the central segment (3–4%). *Golombek et al.* [1996] obtained strain values of 2–3% for extension of the entire Tempe Terra region. *Wilkins et al.* [2002] estimated strain rates in the range 10^{-19}–10^{-20} s^{-1} for the whole Tempe Terra, which parallels the slow deformation rates measured on terrestrial stable intraplate regions. A NW-SE extension direction has been assumed for Tempe Rift and the entire Tempe Fossae by the previous works [e.g., *Mège and Masson*, 1996b; *Hauber and Kronberg*, 2001; *Wilkins et al.*, 2002].

[8] Therefore the Tempe Rift is a large Martian structure, located at a persistently active tectonic region of the planet (northeastern Tharsis dome), from which there exists an excellent previous geological knowledge. These characteristics make Tempe Rift a very suitable place to perform a detailed structural analysis to characterize its fault population patterns and statistics.

3. Methodology

[9] A mosaic of Viking Context Images with a typical resolution of 231 m pixel^{-1} has been used for this structural study. The selected area approximately coincides with the Tempe Rift as defined by *Hauber and Kronberg* [1999, 2001], and it covers a surface of around 335,000 km^2, elongate in a NE-SW trend and centered at coordinates

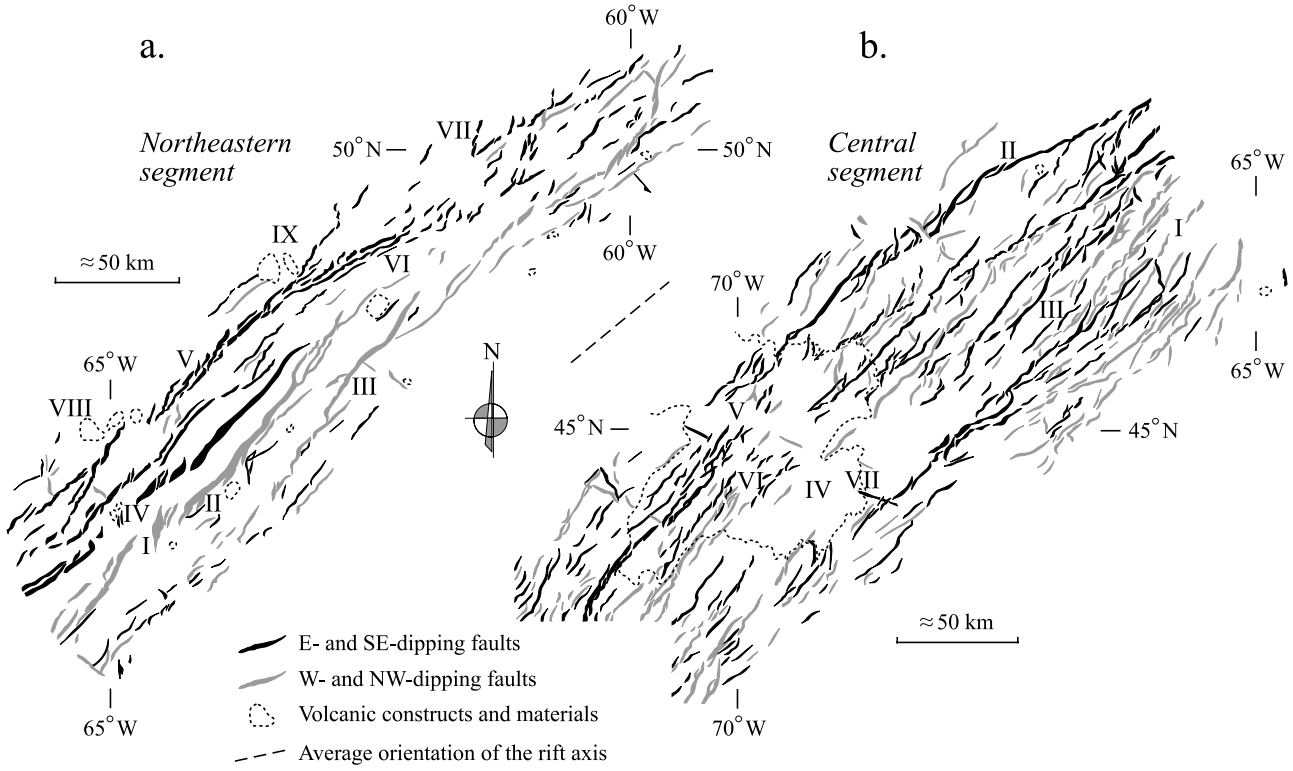

Figure 3. Detailed fault maps of the northern part of the Tempe Rift. Mercator projection. Volcanic edifices and materials are also represented. (a) Northeastern segment. (b) Central segment.

42°N 72°W (Figures 1 and 2). *Hauber and Kronberg* [2001] subdivided the Tempe Rift into three segments (northeastern, central and southwestern) according to their distinct morphological and structural characteristics. This division has been accepted and followed in our work (Figure 2). However, two zones have been distinguished here in the southwestern segment (A and B), due to the contrasted fault patterns exhibited at each zone, as explained below.

[10] Geological photointerpretation of the image mosaic allowed accurate drawing of fault trace maps in Mercator projection (Figures 2, 3, and 4). All observed fractures have been recorded and the resulting maps have been analyzed on a Macintosh computer using the public domain NIH Image program (developed at the U.S. National Institutes of Health and available on the Internet at http://rsb.info.nih.gov/nih-image/). This software allows measurement of the xy coordinates of fault tips and it automatically computes the tip-to-tip fault trend and length (L), which are considered as fundamental parameters of fault characterization [e.g., *Clifton et al.*, 2000]. The program also yields the coordinates of fault centroids (Figure 5, center of the fault ellipse projected onto the structural level of observation [*Ackermann et al.*, 2001]). Fault spacings (S) were measured manually along scanlines oriented normal to the dominant fault strike (Figure 5) [e.g., *Ackermann et al.*, 2001]. Mercator projection is conformal such that it maintains all the angular relationships. A spreadsheet was used for latitude correction of lengths and areas. Measurement problems mainly concern data truncation and censoring [*Schultz and Fori*, 1996; *Ackermann et al.*, 2001]. Truncation is a sampling artifact that affects small faults whose maximum exposed length and displacement is below the resolution of the image. Conventional Viking images do not allow observation of linear features less than 1 km long [*Schultz and Fori*, 1996], yet the resolution limit in our studied zone seems located at around 4 km. Other sampling artifacts are due to exposure characteristics and sampling area dimensions, which include curtailment (faults exceeding the measurement area) or other types of censoring and overprinting by crater impacts, volcanic or sedimentary formations. The selected area was oriented in NE-SW direction to minimize the effects of curtailment (Figure 2). Moreover, the fault traces that became crosscut by the rather arbitrary segment boundaries were prolonged up to their visible length. Volcanic materials coeval to late with respect to faulting are only abundant in the southwestern-B segment and must be considered when interpreting that zone. Except for these problems, the slow rate of Martian erosion and deposition renders an almost intact faulted landscape that strongly recalls the images taken from results of scaled physical models. Apart from this, some truncation and curtailment bias is apparent in the fault statistics, a subject that will be discussed later in this work.

[11] MOLA information has been gathered to construct a series of transversal profiles across the Tempe Rift (Figure 6, profiles a to x) and two longitudinal profiles at selected places of the northeastern segment (Figure 6, profiles y and z). These profiles add valuable information on the three-dimensional geometry of the Tempe Rift. MOLA data have also been used in combination with fault trace maps to obtain an estimation of fault displacements. The procedure is that explained by *Wilkins et al.* [2002]: maximum vertical

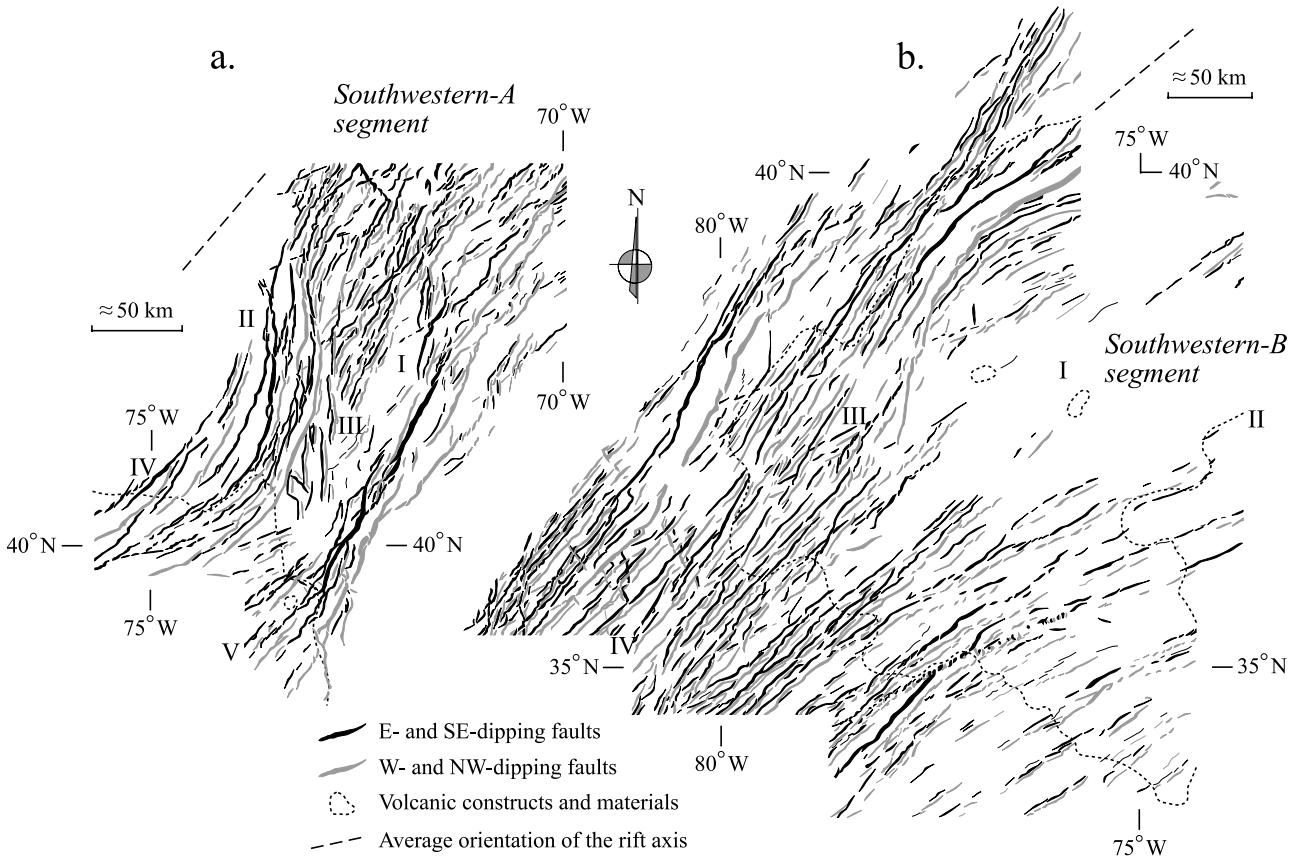

Figure 4. Detailed fault maps of the southern part of the Tempe Rift. Mercator projection. Volcanic edifices and materials are also represented. (a) Southwestern-A segment. (b) Southwestern-B segment.

relief determined along profiles normal to fault strike yield a minimum magnitude of fault throw. Fault displacement is considered as dip-slip, an assumption that holds even under oblique rifting, as shown later in this work. Fault dip is fixed at 60°, although a 10° variation has not resulted in appreciable changes [see also *Wilkins et al.*, 2002].

[12] Collected data have been analyzed using geometric, statistical and fractal methods. Geometry of faults and fault systems has been carefully studied by comparison with experimental analog models. Displacement-length scaling relations for faults on Tempe Rift have been represented in log-log plots of maximum displacement and length data [e.g., *Cowie and Scholz*, 1992] and the results are compared with previous determinations on Mars [*Schultz et al.*, 2006]. Fault trends have been analyzed using fault azimuth histograms whose frequencies were weighted according to fault length [e.g., *Tron and Brun*, 1991; *Bonini et al.*, 1997], and fault length versus fault azimuth graphs [e.g., *Clifton and Schlische*, 2001]. Fault lengths were also represented in log-log or log-linear plots of cumulative frequency. The cumulative number of faults (N^*) having lengths $\geq L$ has been normalized with respect to a reference area according to *Schultz and Fori* [1996]. Fault linkage of closely spaced en échelon fault segments has not been explicitly treated in this work [e.g., *Wilkins et al.*, 2002], such that only independent fault length populations have been considered here. The study of the spatial distribution of fault centroids followed the approach of *Ackermann et al.* [2001] based in turn on *Cressie* [1993] and *Swan and Sandilands* [1995]. This method compares the mean observed nearest neighbor distance between centroids (d(NN)) with that derived from a random distribution (d(ram)). The ratio d(NN)/d(ram) can be used as a nearest neighbor index (*NNI*) to evaluate deviation from uniformity of the spatial distribution of faults. Fractal analysis of fault trace maps was evaluated from a box-counting method. This method determines the number (n) of boxes of a given linear size necessary to cover the studied object. There is a vast amount of literature devoted to this topic, but for further details, see, e.g., *Vignes-Adler et al.* [1991] and *Ackermann et al.* [2001]. Fractal sets follow a power law box size-frequency distribution, where the exponent is $-D$ (capacity dimension, which is a kind of fractal dimension). The analyzed areas did not extend beyond the mapped areas [*Walsh and Watterson*, 1993]. In fault patterns, $D = 2.0$ is indicative of homogeneity and $D < 2.0$ points to a more localized fault concentration [*Cowie*, 1998, and references therein]. Finally, comparison between the histograms of fault directions and the statistical data from the experimental models of *Tron and Brun* [1991] allowed a semi-quantitative estimation of the extension direction across the rift zone [see also *Bonini et al.*, 1997; *Dauteuil et al.*, 2001]. The experimental diagram of *Tron and Brun* [1991] plots the obliquity angle (angle between the extension direction and azimuth of the rift axis) against the fault azimuth centered on the rift axis trend. Shaded areas in this diagram mark the

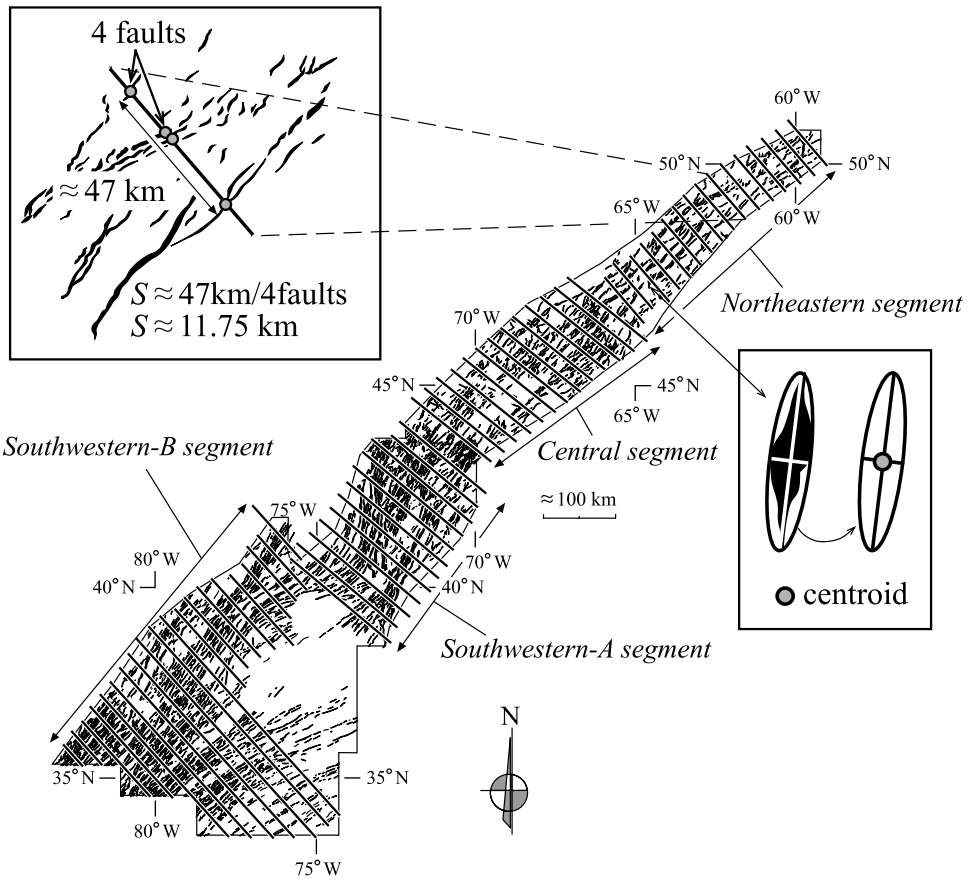

Figure 5. Location of scanlines used to measure the average fault spacing at each segment of the Tempe Rift. The average spacing (S) was determined for each scanline, for instance, along the profile shown in the top left inset, and then all scanlines are averaged to obtain S_{avg} (see main text and Table 1). The right inset illustrates an example of measurement of the xy coordinates of a fault centroid as the center of the best fit ellipse of a given fault. Reference map, Mercator projection.

most frequent orientation span of faults obtained in the experiments. Best fit between the main peaks and significant range of the histograms of fault directions at Tempe Rift and the shaded areas of the experimental diagram allows the optimal obliquity angle, thus the extension direction to be approximately determined.

4. Results

[13] Fault architecture of Tempe Rift is described here using two distinct approximations. First, a detailed qualitative analysis of the geometry of faults and fault systems in plan view and in profile is presented for each rift segment. And second, a statistical study is provided to better characterize the fault populations and to find relevant scaling properties. In this work, fault analysis involves determination of fault scaling relationships, which statistically describe the size and spatial patterns of fault populations [e.g., *Cowie*, 1998].

4.1. Fault and Fault System Geometry: Spatial Patterns of Faults

[14] The northeastern segment is characterized by a well-developed single rift valley that disappears to the north (Figure 6, profile a) against the dichotomy boundary [*Hauber and Kronberg*, 2001]. NW-dipping faults are located at the southeastern rift flank and show large throws, reaching more than 3,000 m (Figure 6, profile e), while SE-dipping faults (northwestern flank) reveal shorter displacements, showing the asymmetric geometry of the rift [*Hauber and Kronberg*, 2001]. An elongate, deep basin is observed in the rift center (Figure 2 and Figure 6, profiles c to e). In plan view, the most striking feature is the absence of any continuous rift-border fault system. The segmented and discontinuous geometry of fault systems leads to rather short lengths of individual faults that do not exceed 150 km. The southeastern master fault system is defined by two main fracture alignments, which show a branched and segmented internal geometry (Figure 3a). These fault sets are oriented parallel to the rift axis. Typical structures are right-stepping, en échelon faults with relay ramps between overlapping segments that inhibited the along-strike propagation of faults (Figure 3a, point I), abandoned splays (Figure 3a, point II) and wavy and kinked shape of fault traces (Figure 3a, point III) indicative of segmented fault systems [e.g., *Clifton et al.*, 2000]. The topographic profile y (Figure 6) approximately runs from point I to II showing the stepped arrangement of fault scarps (arrows in the profile). Three main fault alignments form the northwestern flank of the rift [see also *Hauber and Kronberg*, 2001]. They

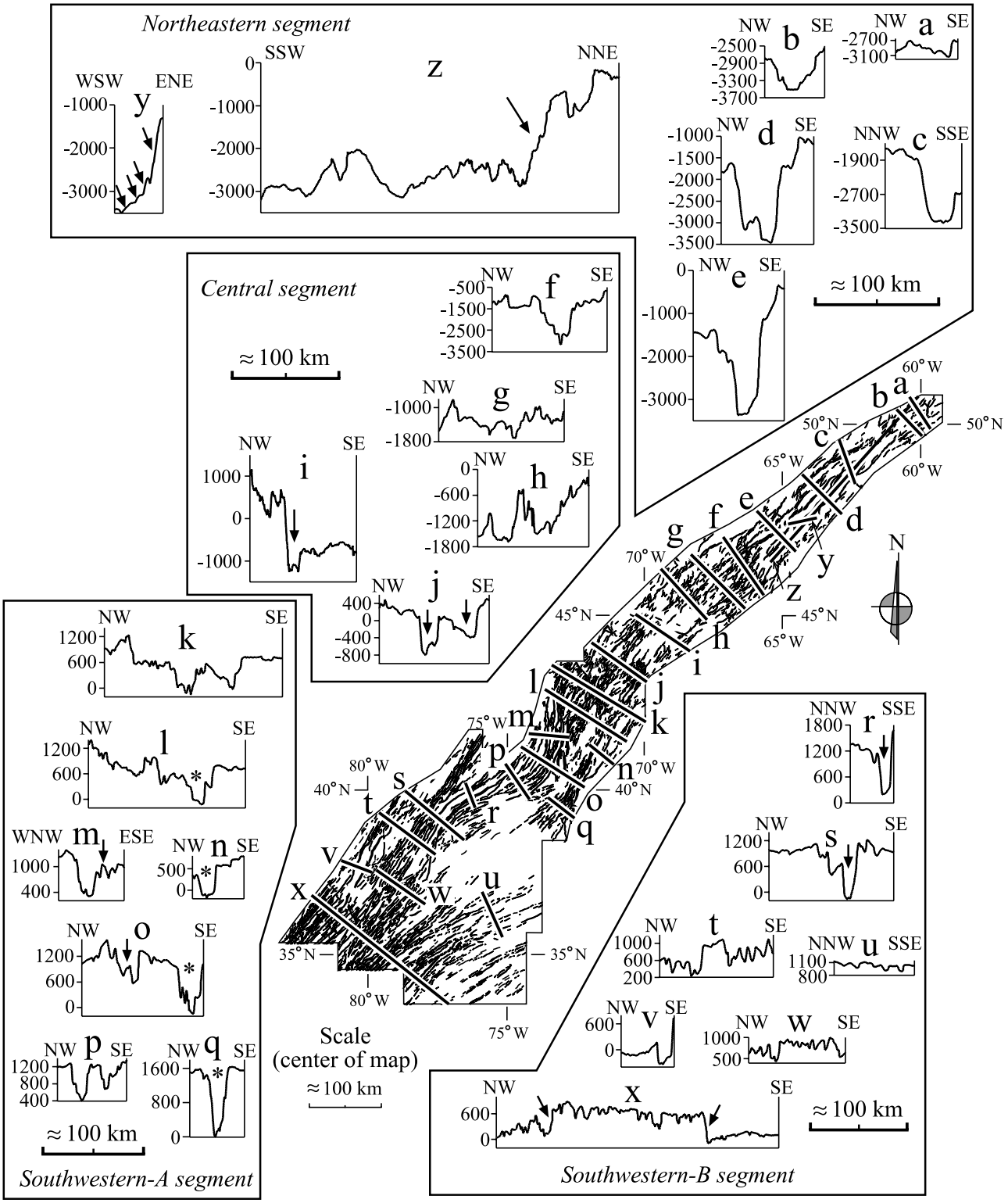

Figure 6. MOLA profiles across and along the Tempe Rift. Arrows and asterisks mark topographic features that are cited and discussed in the main text. Reference map, Mercator projection.

show the same structural characteristics than the fault systems on the opposite side of the rift, with typical right-stepping, en échelon faults (Figure 3a, point IV). Of particular interest is the northwestern border fault system, which shows a double alignment of en-échelon faults partly linked through an intricate pattern of relay ramps (Figure 3a, point V). Fault polarity switching is also visible in some sites, in particular to the north of this area, where a prominent soft-linked accommodation zone (in the sense of, e.g., *McClay et al.* [2002]) sub-parallel to the rift axis can be observed

(Figure 3a, point VI). Soft-linked accommodation zones are formed where groups of like-dipping faults met groups of oppositely dipping faults. This contrasts with the classical transfer faults separating oppositely dipping fault sets, which can be defined as hard-linked accommodation zones [*McClay et al.*, 2002]. Soft-linked accommodation zones can be classified into low-relief and high-relief zones (see again *McClay et al.* [2002] for more information). Low-relief accommodation zones show opposite-polarity faults that rotate into parallelism with the accommodation zone. High-relief accommodation zones are composed of interlocking opposite-polarity fault arrays. According to these definitions, the accommodation zone at point VI of Figure 3a, which marks the northeastern termination of the deep central basin, corresponds to a right-stepping, low-relief oblique accommodation zone, with curved and interlocking extensional fault tips. The central and southwestern part of profile z (Figure 6) strikes parallel to the central basin and it crosses some faults and volcanic constructs. The oblique accommodation zone appears in this profile as a prominent, stepped slope (marked with an arrow) defined by several small faults. To the north of this accommodation zone, faults display two distinct trends, one sub-parallel to the rift axis ($\sim$N50°E), and the other with $\sim$N10°E trending, oblique intra-rift faults (Figure 3a, point VII). Structural differences between the areas to the north (profiles a and b) and south (profiles c to e) of the accommodation zone are clearly marked in the topography (Figure 6). As stated before, small volcanic constructs appear dispersed along this northeastern segment. The most important volcanic edifices are aligned and located in geographical association with the northwestern fault alignment (Figure 3a, points VIII and IX), which suggests a tectonic control on volcanism, already proposed by *Hauber and Kronberg* [2001].

[15] At the southern end of this northeastern segment, its transition with the central segment is rather sharp (Figures 2 and 3; also compare profiles e and f of Figure 6). The main faults limiting the central basin of the northeastern segment branch southward, reducing their relative throws and giving place to a complex, compartmented basin (Figure 3b, point I, and Figure 6, profiles f and g). The resulting small sub-basins align oblique with the large northern basin and with the rift axis. The other NW- and SE-dipping faults of the northeastern segment experience similar changes toward the central segment. The only structure that keeps its structural continuity and geometrical characteristics is the northwestern fault alignment, which shows a curvilinear trace (Figure 3b, point II). This explains the change in the location of the master fault system that passes to the northwestern rift border at this central segment, a feature already observed by *Hauber and Kronberg* [2001]. There is no evidence of any structure that could have acted as transfer fault (hard-linked accommodation zone) in the boundary between the northeastern and central segments. The structural architecture of this boundary, with presence of branching and curvilinear fault sets, can be tentatively described as a soft-link, low-relief accommodation zone (see definitions above in this section).

[16] As a whole, the central segment shows a larger fault density than the northeastern one (compare Figures 3a and 3b). Lengths of individual fault segments do not exceed 100 km, a value that coincides with the mean rift width at this zone [*Hauber and Kronberg*, 2001]. No predominant central basin can be observed. Instead, conjugate systems of short right-stepping, en échelon faults, and abundant fault polarity switching, give place to small rhomboidal horsts and graben (Figure 3b, point III). Particularly interesting is the volcanic region located at the southern part of this central segment (Figure 3b, point IV). *Hauber and Kronberg* [2001] noted the early to synrift age of the volcanic activity in this area. A striking change in fault pattern takes place at this volcanic center. The northwestern master fault system appears branched and displaced (Figure 3b, point V) but it shows no apparent curvature. Other fault systems show interlocking of oppositely dipping fault tips (Figure 3b, point VI). Profiles i and j (Figure 6) show the presence of a few deep graben (arrows in the profiles), which contrasts with the more compartmented geometry observed to the north of the volcanic zone (profiles g and h). *Hauber and Kronberg* [2001] explained this change in the internal structure of the rift as due to a possible transfer zone (hard-linked accommodation zone), of which the small N70°W trending faults observed in this area could represent isolated fragments or associated faults (Figure 3b, point VII). However, the available images do not allow recognizing a clear strike-slip or oblique-slip major transfer fault. The described geometrical features (interlocking of oppositely dipping, straight fault sets) point rather to a soft-linked, high-relief accommodation zone, which is therefore the interpretation favored here.

[17] The fault pattern at the northeastern half of the southwestern-A segment shows similar characteristics with respect to that at the central segment, of which it seems merely a southern prolongation (Figure 6, compare profiles j and k). Therefore en échelon fault systems, small soft-linked accommodation zones and rhomboidal graben and horsts are common in this area (Figure 4a, point I). What distinguishes this segment from the central segment is the presence at its western half of a huge sigmoid, an S-shaped rift-border fault system (Figure 4a, point II). The along-strike length of this structure exceeds 200 km and it shows a maximum width of around 30 km. It shows a complex internal structure with a central horst (Figure 6, profiles m and o; the arrows mark the horst). Faults that limit the main sigmoid system are long, curved and almost continuous, although local stepped and tortuous traces suggest fault segmentation. Faults at the northern tip of this sigmoid system smoothly link with the NE-SW trending faults typical of the northeastern part of this segment. At its central part, where the sigmoid system trends approximately N-S, it interrupts the trace of the NE-SW trending faults, although these faults merely fade out before encountering the sigmoid system, and no clear crosscut relationship among them can be observed (Figure 4a, point III). Small N-S oriented graben can be observed in this zone (point III). The sigmoid fault system branches southward into a right-stepped pattern of curved graben and horsts (Figure 4a, point IV) that give place without continuity solution to the fault systems of southwestern-B segment (Figure 6, profile p). On the other side, a deep, straight, symmetric NE-SW graben outlines the eastern boundary of this segment (Figure 6, marked with an asterisk in profiles l, n, o, and q). As a whole, the southwestern-A segment exhibits a

width similar to that of the central segment, a feature that drastically changes toward the southwestern-B segment.

[18] Fault systems are partly covered by volcanic materials at the southern tip of the southwestern-A segment. At least three major volcanic centers can be observed in this zone (Figure 4a, point V, and Figure 4b, point I), which were active syn- to postrift as shown by *Hauber and Kronberg* [2001]. The fault systems at the southwestern-B segment diverge embracing the area covered by the volcanic materials (with center near point I of Figure 4b), although the southeastern part of this curved pattern appears somewhat effaced (Figure 4b, point II). A prominent graben can be observed embracing the volcanic area at the north of this segment (Figure 6, arrows in profiles r and s). This geometry has been described as a ring-like fracture pattern and compared to Alba Patera and Venusian coronae by *Watters and Janes* [1995]. Apart from this feature, faults in the southwestern-B segment are mostly straight, and en échelon systems are scarcely seen, albeit not completely absent (Figure 4b, point III). Similarly, along-strike faults variations and rhomboidal basins are rare but present (Figure 4b, point IV). The southern half of the segment can be best described as a system of parallel, N40°–50°E trending graben spanning rather homogeneously the entire rift width (more than 300 km, see also *Hauber and Kronberg* [2001]). Individual graben are narrow (<5 km) (Figure 6, profiles t to x) and short (<100 km). The main topographic feature of this area is a large plateau (Figure 6, profile x) standing out more than 500 m over its surrounding plains. Both the northwest and southeast boundaries of the plateau are sharp and marked by faults (arrows in profile x). Systems of crosscutting and apparently younger NW-SE, ENE-WSW and N-S fractures become predominant to the south and outside the mapped area. This feature and the presence there of recent Tharsis lavas covering the old rift justify the location of the southern limit of this study.

4.2. Fault Scaling Relationships

[19] Plots of maximum fault displacement against fault length are represented in Figure 7. Contouring of point density reveals interesting characteristics of the measured data. Maximum density areas are elongate and sub-parallel to the lines of constant ratio of maximum displacement to length (oblique, dashed lines at Figure 7), evidencing that the displacement-length relationship is linear, a feature already observed on Earth and Mars [*Cowie and Scholz*, 1992; *Schultz et al.*, 2006]. Approximate values of the maximum displacement-length ratio (γ) can be given from the location of the high-density areas in the diagrams, and they vary from near 10^{-2} (central and southwestern-A segments, Figures 7b and 7c), to around $6-7 \times 10^{-3}$ (northeastern and southwestern-B segments, Figures 7a and 7d). A secondary maximum can be observed in the northeastern segment with a γ value of $3-4 \times 10^{-2}$. Statistic determination of the γ value is not significant due to the large scatter of data, which yields low correlation coefficients. Comparison of the maximum displacement-length data from Earth and Mars (Figure 8) shows that Martian normal faults exhibit lower γ values and hence smaller values of displacement than terrestrial faults. Interpretation of these features will be given in the discussion section.

[20] Histograms and polar diagrams of fault azimuths are markedly skewed (Figure 9). The asymmetry of azimuth frequency diagrams is larger for the central and southwestern-A segments, while the histogram of the southwestern-B segment is more symmetric. In absence of a well-defined axial valley along most of the Tempe Rift, the rift axis has been determined as an ideal line trending parallel to the long axis of the elongate zone defined by the concentration of faults and graben at each segment (Figure 2). Fault azimuth representations are unimodal, with the main peak slightly rotated counterclockwise with respect to the rift axis at each segment. Again, this obliquity attains a maximum at the central and southwestern-A segments, and it is minimum at the southwestern-B segment (Figure 9). Length versus azimuth diagrams (Figure 10) show that rift axis sub-parallel faults are short at the central and southwestern-A segments (open squares, Figures 10b and 10c), and that the largest faults generally coincide with the most frequent fault trends, systematically located to the west of the rift axis (gray squares, Figures 10b and 10c). Instead, long faults are mostly sub-parallel to the rift axis at the northeastern and southwestern-B segments (open squares, Figures 10a and 10d), albeit a tendency of a few long faults to strike counterclockwise to the rift axis is also observable (gray squares, Figures 10a and 10d). At the northeastern segment, the long faults sub-parallel to the rift axis coincide with those defining the deep central basin. The southwestern-B segment shows a symmetric arrangement of points (the axis of symmetry is only slightly rotated counterclockwise with respect to the rift axis; Figure 10d), which contrasts with the other zones that exhibit low-populated zones or even gaps (i.e., complete absence of faults bearing those azimuths) to the east of the rift axis (Figures 10a to 10c).

[21] A summary of fault scaling results (apart from γ values) is presented in Table 1. Fault lengths and spacing recorded in Table 1 have been rounded to the nearest integer number in agreement with the average resolution of the images. The average observed fault length (L_{avg}, arithmetic mean of fault lengths at each segment) and the maximum observed fault length (L_{max}) attain maximum values at the southwestern-A segment (17 km), which is the segment with the longest faults in the Tempe Rift. High L_{max} values are also observed at the northeastern segment that shows, in contrast, the shortest L_{avg} value. This signifies that the northeastern segment is dominated by short faults. Similar results are obtained with the L_{95} parameter that is the 95th percentile of the fault lengths. However, the L_{95} value of the northeastern segment is the largest, which evidences the presence here of a significant group of long faults (those limiting the large central graben), which are even more abundant than at the southwestern-A segment. The influence of many short faults strongly reduces the L_{avg} value of the northeastern segment, as mentioned before. The other two segments exhibit intermediate average fault lengths and small L_{max} and L_{95} values, indicating less dispersed fault-length distributions and the absence of long faults. The southwestern-B segment shows the greatest values of ΣL (the sum of the lengths of all faults at each segment) and ΣL/area, i.e., more than 13,000 km and around 0.11 km per km^2, respectively, which indicates that this segment has the

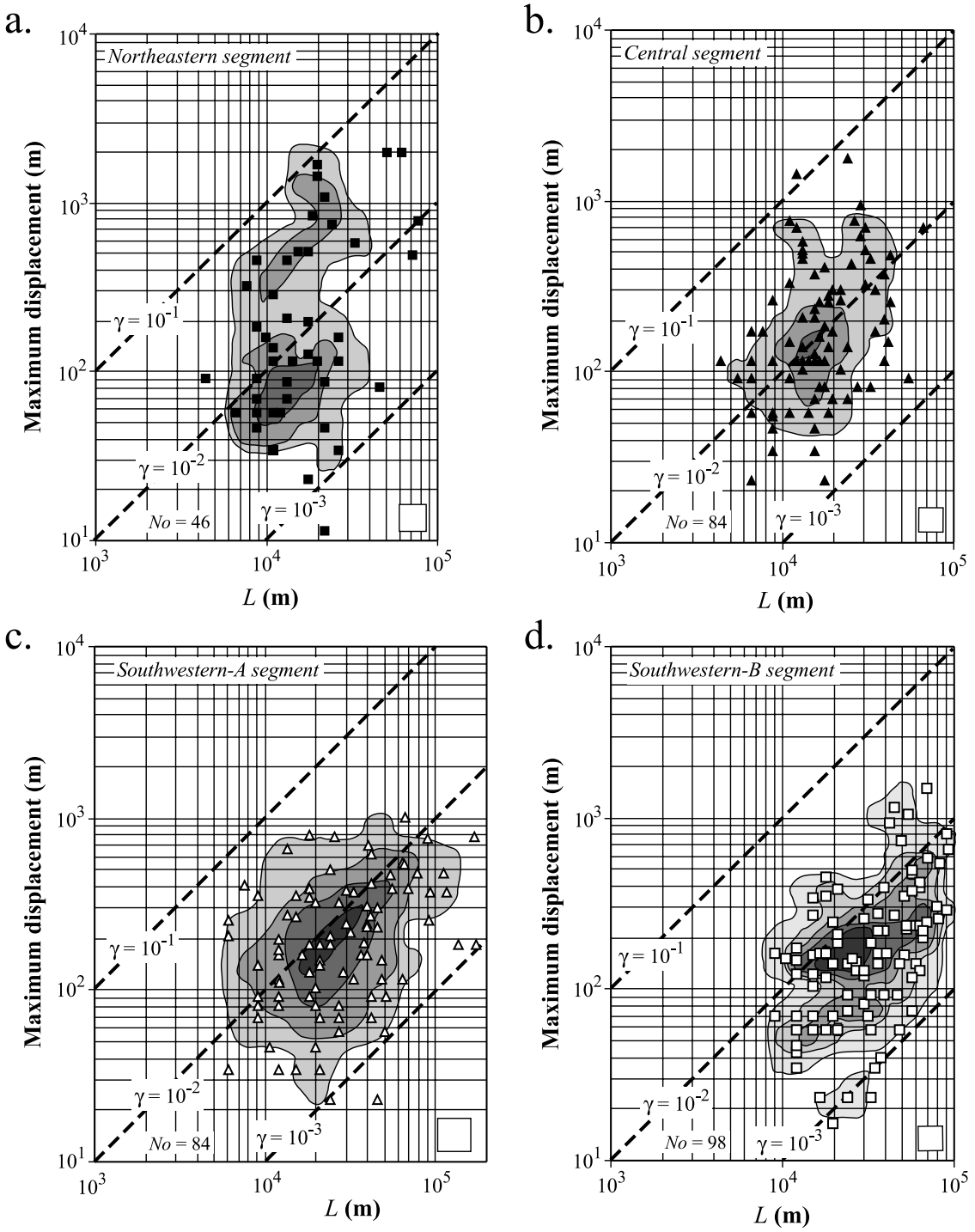

Figure 7. Log-log plots of fault maximum displacement against fault length (L). The oblique, dashed lines represent distinct values of the ratio displacement/length (γ). Contours of point density have been generated following standard techniques in structural geology widely used for contouring spherical orientation data [e.g., *Robin and Jowett*, 1986]. The size of the counting areas is indicated by the small white square located at the bottom right corner of each diagram. *No* is the number of measured faults. (a) Northeastern segment. Contour interval: 3%. (b) Central segment. Contour interval: 4%. (c) Southwestern-A segment. Contour interval: 4%. (d) Southwestern-B segment. Contour interval: 2%.

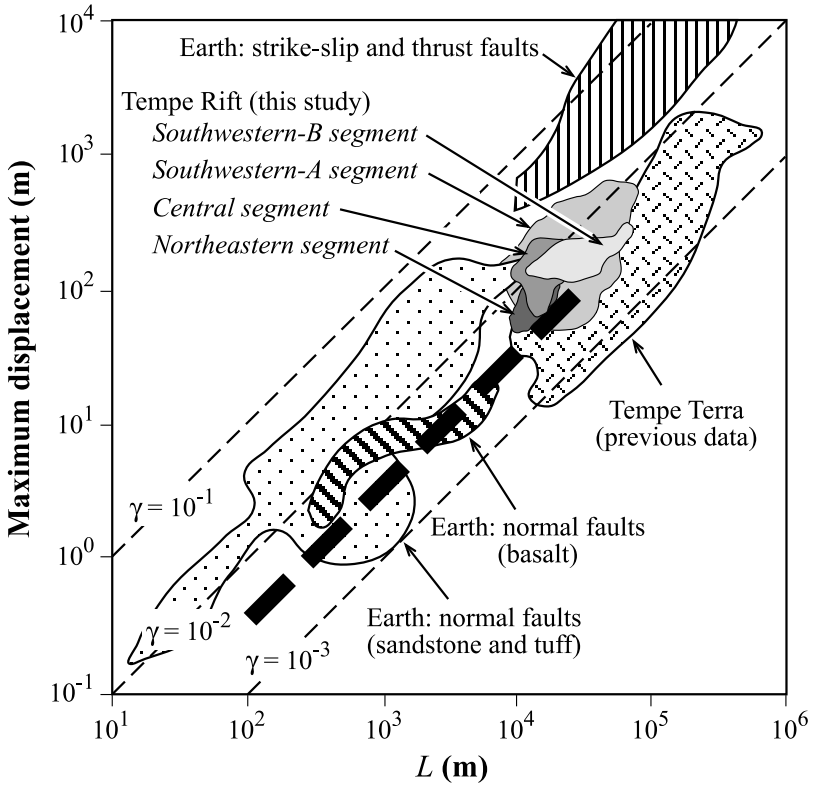

Figure 8. Log-log plot of fault maximum displacement against fault length for normal faults from Earth and Tempe Terra (data from *Schlische et al.* [1996], *Wilkins et al.* [2002], and *Hauber and Kronberg* [2005]). Compilation of long (>10 km) terrestrial strike-slip and thrust faults by *Cowie and Scholz* [1992]. Representative data from this work are plotted as the high-density areas enclosed by the 9% (Northeastern segment) and 8% (rest of segments) contour curves (see Figure 7). Thin, dashed straight lines represent the ratio displacement/length (γ). The thick, dashed line corresponds to the calculated displacement/length scaling relation for Mars basaltic rocks according to *Schultz et al.* [2006].

densest fault concentration of the Tempe Rift. By contrast, the northeastern segment shows the smallest values of these parameters. Therefore fault density progressively decreases from southwest to northeast.

[22] Correlation coefficients suggest that cumulative size-frequency distribution of fault lengths is better described by an exponential than by a power law relationship at the four studied segments (Figure 11 and Table 1). The straight log-linear size-frequency plots (Figure 11a) contrast with the curved central part of the log-log size-frequency plots (Figure 11b), which suggests that the fault-length distributions are not well described by power law functions. Curtailment, overprinting and truncation are probably present at Figure 11b, but they are not responsible for the central curved part of the log-log plots. Parametric (χ^2) and non-parametric (Kolmogorov-Smirov) goodness-of-fit tests have been applied (Table 1). Fit to an exponential function cannot be rejected at any zone (significance level, 0.05). Fit to a power law relationship is rejected at this significance level for fault populations at the central and southwestern-B segments. The tests did not yield rejection to power law functions for the faults of the northeastern and southwestern-A segments, but the calculated test statistics are near the rejection critical values. Although not shown on Table 1, goodness-of-fit to normal and log-normal distributions has been checked and rejected at the same significance level.

[23] Average fault spacing (S_{avg}) progressively decreases from northeast to southwest (Table 1). The average standard deviation of fault spacing also decreases in the same direction indicating that fault spacing becomes more regular. The slight increase of the standard deviation at the southwestern-B segment is due to the presence of syn- and postrift volcanic materials. The calculated nearest neighbor index (*NNI*) that measures the spatial distribution of fault centroids has similar values at the four studied segments (Table 1). These values are well below 2 (uniformity) and even 1 (randomness), but are larger than 0 (clustered point pattern). In fact, rejection of randomness has been verified with a two-tailed Z-test, whose statistics are shown in Table 1, while the critical value is of -1.96 (level of significance, 0.05). As long as the statistics are well within the rejection region, the randomness hypothesis is rejected in all the studied zones.

[24] Use of the box-counting method to assess the fault map patterns suggests that the maps of the four studied segments are fractal (Figure 12). Correlation coefficients are larger than 0.998 (Table 1). The capacity or fractal dimension ranges from 1.55 (northeastern segment) to 1.7 (southwestern-A segment), which can be interpreted as the result of inhomogeneous, localized deformation [*Cowie*, 1998].

[25] Histograms of fault azimuths have been compared with the experimental data of *Tron and Brun* [1991] to

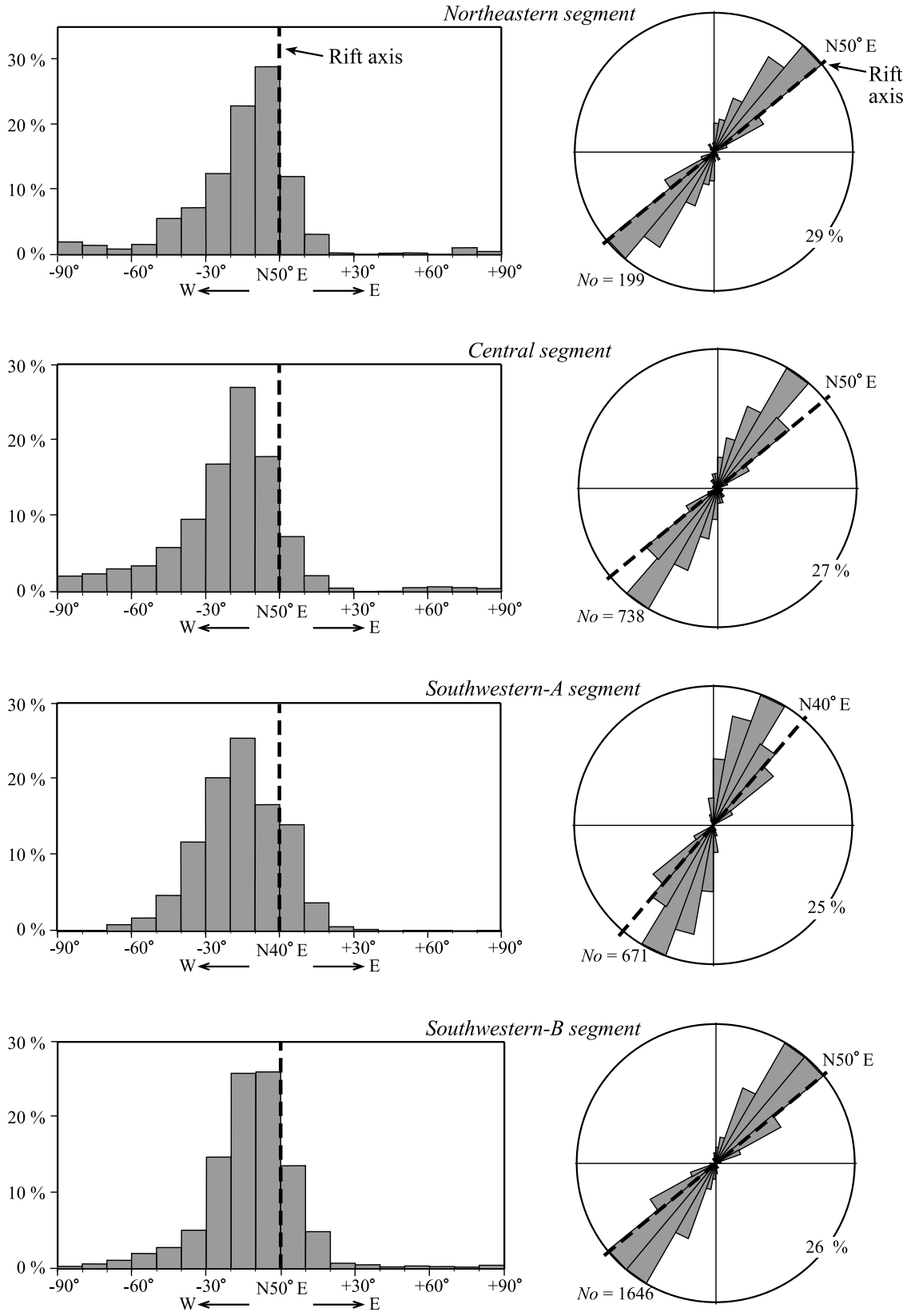

Figure 9. Histograms of fault azimuths (left column) and polar diagrams of fault azimuths (right column) of the four studied segments. The rift axis (dashed lines) is taken as the reference azimuth. The value of one direction of the histogram or pole diagram is the sum of the length of faults that have this orientation. *No* is the number of measured faults. The maximum percentage is indicated at each polar diagram.

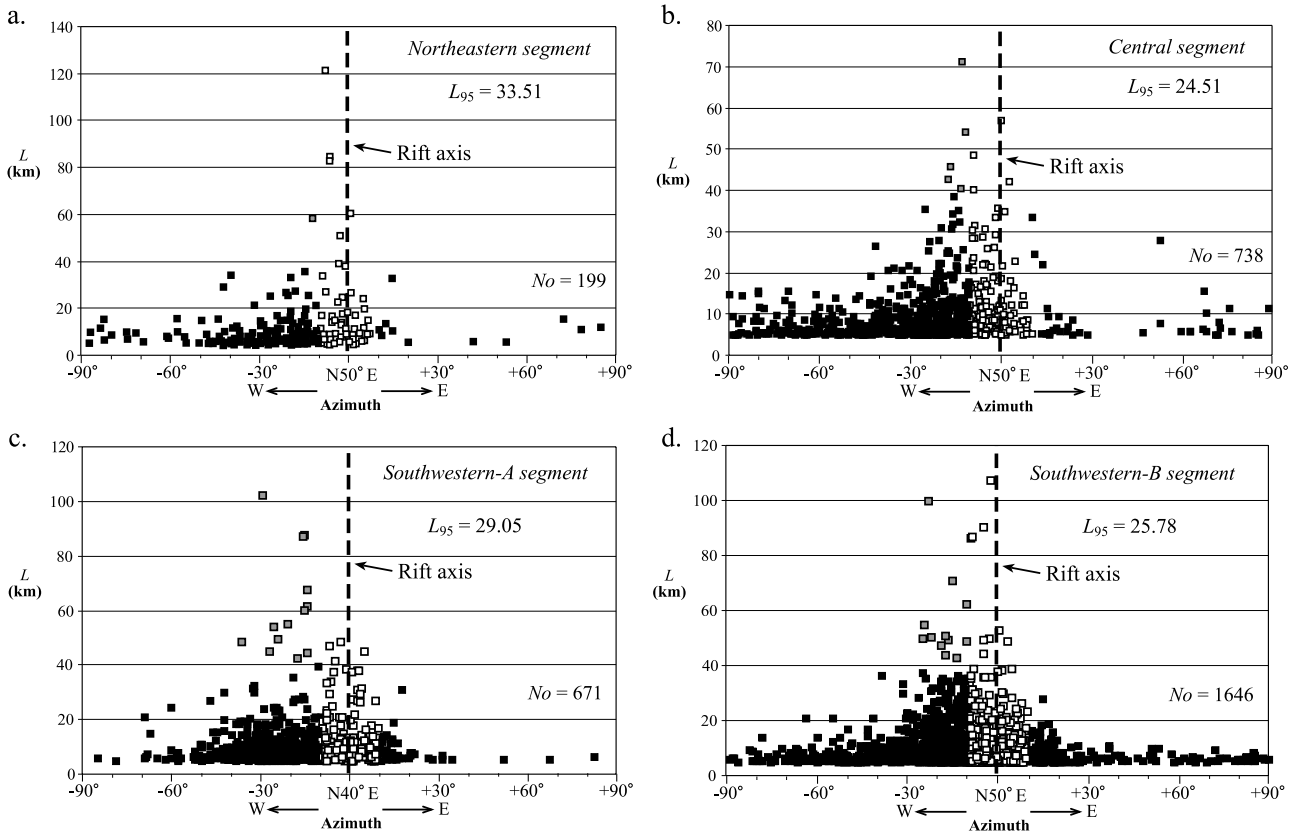

Figure 10. Fault length versus fault azimuth diagrams for the studied zone. The rift axis (dashed lines) is taken as the reference azimuth. Resolution cutoff is around 4 km. L_{95} is the 95th percentile of the fault lengths. *No* is the number of measured faults. Open squares represent faults whose strike deviates less than 10° from the rift axis. Gray squares represent faults whose lengths exceed 40 km and deviating more than 10° counterclockwise from the rift axis. Black squares mark the rest of the measured faults. (a) Northeastern segment. (b) Central segment. (c) Southwestern-A segment. (d) Southwestern-B segment.

obtain the approximate location of the extension direction across the distinct segments of the Tempe Rift. Results indicate (Figure 13 and Table 1) that the angle between the rift axis and the extension direction (α) could have varied from 50°–60° (southwestern-A segment) to 66°–88° (southwestern-B segment).

5. Discussion

5.1. Oblique Rifting at the Tempe Rift

[26] Analog models of extensional fault systems [e.g., *Whithjack and Jamison*, 1986; *Tron and Brun*, 1991; *Keep and McClay*, 1997; *Clifton et al.*, 2000; *McClay et al.*, 2001; *Schlische et al.*, 2002] have considerably improved our understanding of the tectonic evolution of rifts and extensional zones on Earth (e.g., the Gulf of Aden Rift [*Dauteuil et al.*, 2001], the Ethiopian Rift [*Bonini et al.*, 1997], or the Reykjanes Peninsula [*Clifton and Schlische*, 2003]). Numerical, analytical and analog models, and field studies have evidenced that orthogonal and oblique extensions generate quite distinct fault architectures. Further complications include successive orthogonal and oblique extensional episodes (orthogonal to oblique or vice versa) that have been also studied with experimental models [*Bonini et al.*, 1997; *Keep and McClay*, 1997]. Unfortunately, no attempt has been made in the Martian exploration to date to obtain structural insights from available scaled physical models. Oblique rifts present the following diagnostic characteristics with respect to orthogonal rifts [*Whithjack and Jamison*, 1986; *Tron and Brun*, 1991; *McClay et al.*, 2001]: Segmented and en échelon rift border faults parallel to the rift axis, intra-rift fault domains oblique to the rift axis, important structural variation along-axis including fault polarity switching and rhomboidal sub-basins and horst blocks, presence of relay ramps and accommodation zones inhibiting the along-strike propagation of internal faults, frequent curved and sigmoid faults. As described in previous sections, all these elements are present at the Tempe Rift, thus suggesting that it can be considered as an example of extraterrestrial oblique rift. This is particularly obvious for the central and southwestern-A segments, whose fault patterns (Figures 3 and 4) are strikingly similar to those visible in the oblique-rifting experiments of *McClay et al.* [2001, 2002], *Clifton and Schlische* [2001], and *Schlische et al.* [2002]. The northeastern segment shows fault patterns also representing oblique rifting, although the presence of some long sub-parallel faults limiting deep graben seems indicative of low obliquity angles. Instead, the fault pattern at the southwestern-B segment is more similar to those obtained from models of orthogonal rifting.

Table 1. Results of the Fault-Population Analysis in the Tempe Fossae Rift[a]

	Northeastern Segment	Central Segment	Southwestern-A Segment	Southwestern-B Segment
Fault length, km				
L_{avg}	13	16	17	14
L_{max}	150	92	196	107
ΣL	3299	7226	8871	13375
L_{95}	34	25	29	26
ΣL/area, km^{-1}	0.0724	0.0857	0.1029	0.1110
N_o	199	738	671	1646
Cumulative frequency of fault lengths				
Exponential	$N^* = 82.27\exp(-0.134L)$	$N^* = 64.55\exp(-0.080L)$	$N^* = 63.16\exp(-0.066L)$	$N^* = 73.07\exp(-0.071L)$
R^2	0.9895	0.9838	0.9962	0.9893
L_c, km	7	13	15	14
χ^2 test	0.56 (12.59)	10.00 (41.34)	1.05 (19.68)	9.57 (33.92)
K-S test	0.04 (0.43)	0.07 (0.24)	0.08 (0.35)	0.13 (0.26)
Power law	$N^* = 1875.5L^{-1.9965}$	$N^* = 3787.7L^{-2.0174}$	$N^* = 2372.7L^{-1.7348}$	$N^* = 1341.1L^{-1.5699}$
R^2	0.9365	0.9577	0.9553	0.9476
χ^2 test	7.88 (12.59)	59.88 (41.34)	12.18 (19,68)	45.69 (33.92)
K-S test	0.22 (0.43)	0.41 (0.24)	0.22 (0.35)	0.33 (0.26)
Fault spacing, km				
S_{avg}	11	9	6	6
St. dev.	4	3	1	2
Spatial distribution of fault centroids				
d(NN)	6.33	4.28	4.66	4.24
d(ram)	14.99	9.29	6.48	6.78
NNI	0.4225	0.4600	0.7193	0.6245
Z_{test}	−15.5837	−28.0660	−13.9103	−29.14304
Fractal analysis of fault trace maps				
Equation	$n = 9092.2(bs)^{-1.5507}$	$n = 20683(bs)^{-1.585}$	$n = 24461(bs)^{-1.695}$	$n = 32428(bs)^{-1.6041}$
R^2	0.9986	0.9992	0.9985	0.9987
D	1.55	1.59	1.7	1.6
α (obliquity)	60°−75°	52°−70°	50°−60°	66°−88°

[a] L is fault length; L_{avg} and L_{max} are the average and maximum fault length, respectively; ΣL is the sum of the lengths of all faults at each segment; L_{95} is the 95th percentile of the fault lengths, and N_o is the number of measured faults; R^2 is the correlation coefficient for the exponential or power law distribution of the cumulative frequency of fault lengths; L_c is the characteristic length or average fault length assuming exponential distribution; χ^2 goodness-of-fit test and Kolmogorov-Smirnov goodness-of-fit test (significance level, 0.05) to exponential and power law functions: fit is rejected when the statistic exceeds the critical value (between parentheses); S_{avg} is the average fault spacing, and the standard deviation is also expressed; d(NN) is the nearest neighbor distance of fault centroids, and d(ram) is the nearest neighbor distance based on a random distribution; *NNI* is the nearest neighbor index, equal to d(NN)/d(ram); Z_{test} is the statistic of a standard Z two-tailed test devised to analyze the randomness of fault centroids, rejection of randomness is expected when the statistic value exceeds the critical value (−1.96 at 0.05 as level of significance); fractal analysis of fault maps includes the fractal dimension (D) and the correlation coefficient (R^2) of the box-counting straight line (equation is shown); α is the estimated angle between the extension direction and the rift axis.

[27] Additional evidence of oblique rifting comes from the analysis of fault azimuth diagrams (Figures 9 and 10). Experimental results and field-based observations have clearly shown that orthogonal rifting generates symmetric diagrams and that their main peaks parallelize the rift axis. Instead, the strike of the faults is oblique to the strike of the rift axis and histograms are asymmetric under oblique rifting [e.g., *Tron and Brun*, 1991; *Schlische et al.*, 2002]. This is precisely the case for at least three of the studied segments (Figure 9), and only the southwestern-B segment shows diagrams of fault azimuths that can be explained by high-angle oblique or even orthogonal extension. The assertion by *Tron and Brun* [1991] that faults are never normal to the displacement direction in oblique extension was confirmed by *Clifton and Schlische* [2001] and later observed by *Clifton and Schlische* [2003] at the Reykjanes Peninsula. Comparison with the experimental results of *Tron and Brun* [1991] yields obliquity angles (α) clearly indicative of oblique extension, in particular for the southwestern-A segment, where α could be as low as 50°. Although most of the Tempe Rift would have been subjected to oblique rifting, the southwestern-B segment shows the lowest obliquity values (α approaching 88°). Interestingly, the ring-like fractures associated with the large volcano at the north of this segment do not modify the general fault pattern. Transition from orthogonal to oblique extension has been described at the Kenya Rift [see, e.g., *McClay et al.*, 2001], which was compared with the Tempe Rift by *Hauber and Kronberg* [2001]. Projection of the normal to the extension direction at the polar diagrams of fault azimuths (Figure 14) indicates that the modal peak of fault trends is located between that direction and the rift axis, in close coincidence with that observed in experiments and terrestrial cases of oblique rifting [e.g., *Schlische et al.*, 2002; *Clifton and Schlische*, 2003].

[28] In summary, our data unequivocally support oblique extension at the Tempe Rift. This oblique extension could have taken place late during the Noachian, as suggested by *Hauber and Kronberg* [2001] according to the estimated age of the volcanic constructs of the southwestern-B segment (3.51 Ga). Location of volcanic edifices at some particular structural sites of the obliquely rifted zone, as soft-linked accommodation zones, is an evidence of the sharp association between tectonic and magmatic activities, which attests the crustal-scale importance of this rifting process. The large-scale strike-slip component of displacement should have been sinistral at the four studied segments (Figure 14). Contrary to intuition, analog experiments have

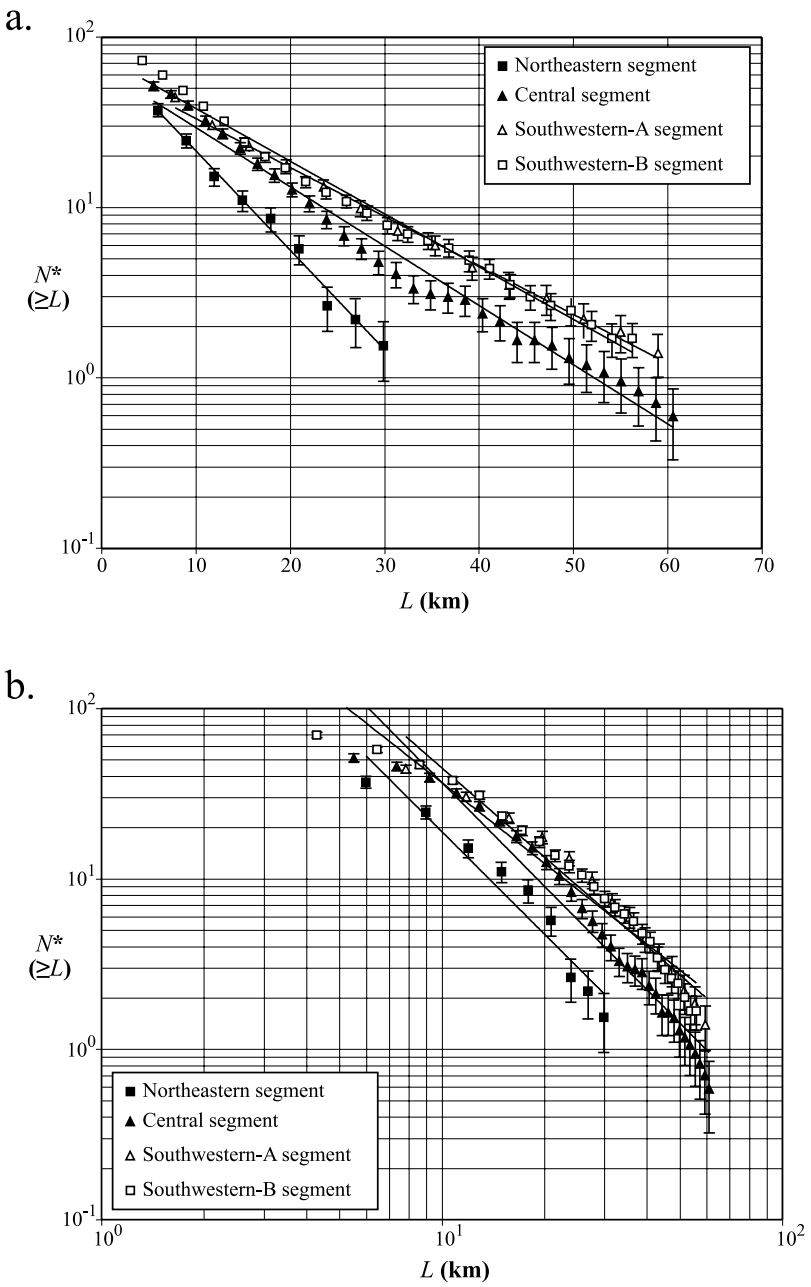

Figure 11. Cumulative number of faults (N*), normalized by reference area versus length (L). Normalization follows the *Schultz and Fori* [1996] proposal for Mars, with $N^* = N \times 10^4/A$, where 10^4 km^2 is the reference area and A is the area (in km^2) of each studied surface containing faults. Northeastern segment: A = 45,594 km^2. Central segment: A = 84,337 km^2. Southwestern-A segment: A = 86,210 km^2. Southwestern-B segment: A = 120,445 km^2. Calculated uncertainties due to population statistics (error bars) are $\pm 1\sigma$, with $\sigma = [\Sigma N^* \times (10^4/A)]^{(1/2)}$, where ΣN^* is the cumulative normalized number of faults of given length. (a) Log-linear plots. (b) Log-log plots. Straight lines correspond to best fit regression lines.

proved that faults generated and displaced under oblique extension are pure dip-slip, normal faults [e.g., *Clifton et al.*, 2000]. Strike-slip or oblique faults are only observed under very low α values (<30°). Therefore the previous observations and strain measurement at Tempe Rift assuming dip-slip fault displacements are probably well founded and they not contradict the results of this work. Nevertheless, oblique extension regimes involve generation of several distinct coeval fault trends, a feature profusely described in this work for the Tempe Rift. Under oblique rifting, the presence of two or more coeval fault sets differing in their average trends do not necessarily indicate distinct episodes of regional extension [*Schlische et al.*, 2002]. The lack of evidences for clear crosscutting relationships at our studied zones (Figures 3 and 4) can be interpreted as due to the essentially contemporary nature of these distinct fault sys-

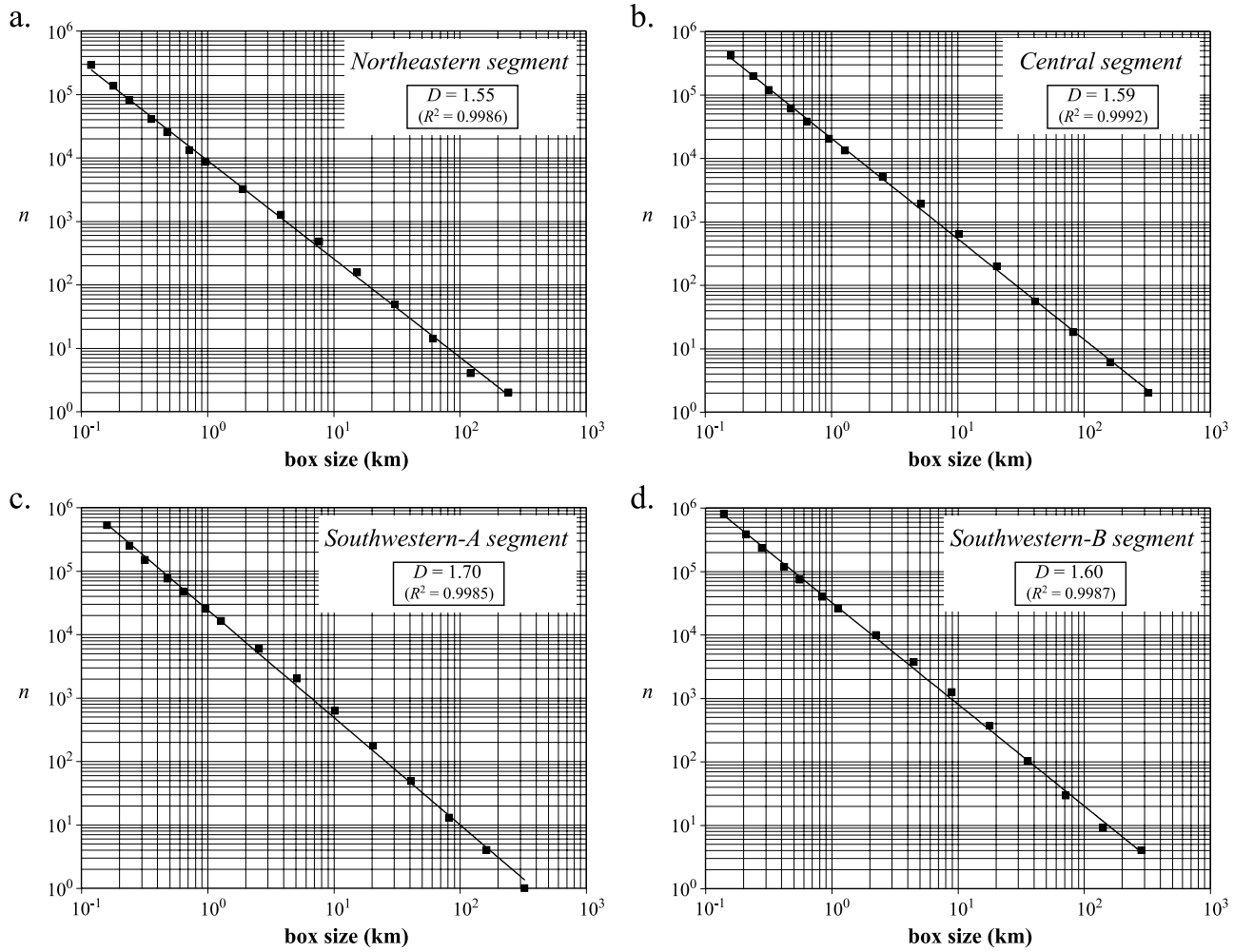

Figure 12. Box counting curves for fracture maps of the four studied segments of the Tempe Rift. Number of boxes occupied by faults (n) is represented against the line size of boxes. The single initial box is completely included within the studied zones. Results show a straight-line distribution over almost four orders of magnitude of box size. Fractal dimension of the distribution is obtained from the slope ($-D$) of the straight line relating n with box size. Correlation coefficient is R^2. (a) Northeastern segment. (b) Central segment. (c) Southwestern-A segment. (d) Southwestern-B segment.

tems. A corollary of this is that some of the tectonic evolution models based on supposedly distinct and successive fault sets differing in their trend could be tentatively reinterpreted in Tempe Terra as perhaps in the rest of the planet. Future high-resolution data can help to check fault crosscut relationships.

[29] On Earth, oblique rifting is probably the rule rather than the exception [*Schlische et al.*, 2002]. This is due, among other causes, to the presence of previous faults acting as structural inheritances of an older deformation phase [*Keep and McClay*, 1997]. Reactivation of preexisting structures impressed in the Tempe Fossae crust was already suggested by *Hauber and Kronberg* [2001] to explain the geometrical characteristics of the Tempe Rift. This is an additional evidence of the long and changing structural evolution of the Tharsis region during the Noachian [*Mège and Masson*, 1996a; *Anguita et al.*, 2006]. Spatial variation in the estimated extension direction (Figure 14) could be due to a deformation field with curved trajectories. However, the data presented in this work rather favor local deviations of the principal deformation axes around crustal-scale major fractures or fractured zones. This feature is particularly evident at the southwestern-A zone, where an anticlockwise rotation of the rift axis is observed, and large sigmoid faults have been generated.

5.2. Implications of the Fault Scaling Relationships at the Tempe Rift

[30] Diagrams of maximum fault displacement against fault length (Figure 7) show a significant scatter that, in some cases, can attain more than two orders of fault-displacement magnitude (e.g., Figure 7a). This scatter is larger than that observed by *Wilkins et al.* [2002] at the entire Tempe Terra (around one order of fault-displacement magnitude). *Cowie and Scholz* [1992] discussed the main sources of scatter in these types of data. A characteristic feature of faults at the Tempe Rift, profusely described in this work, is its segmented geometry and en échelon

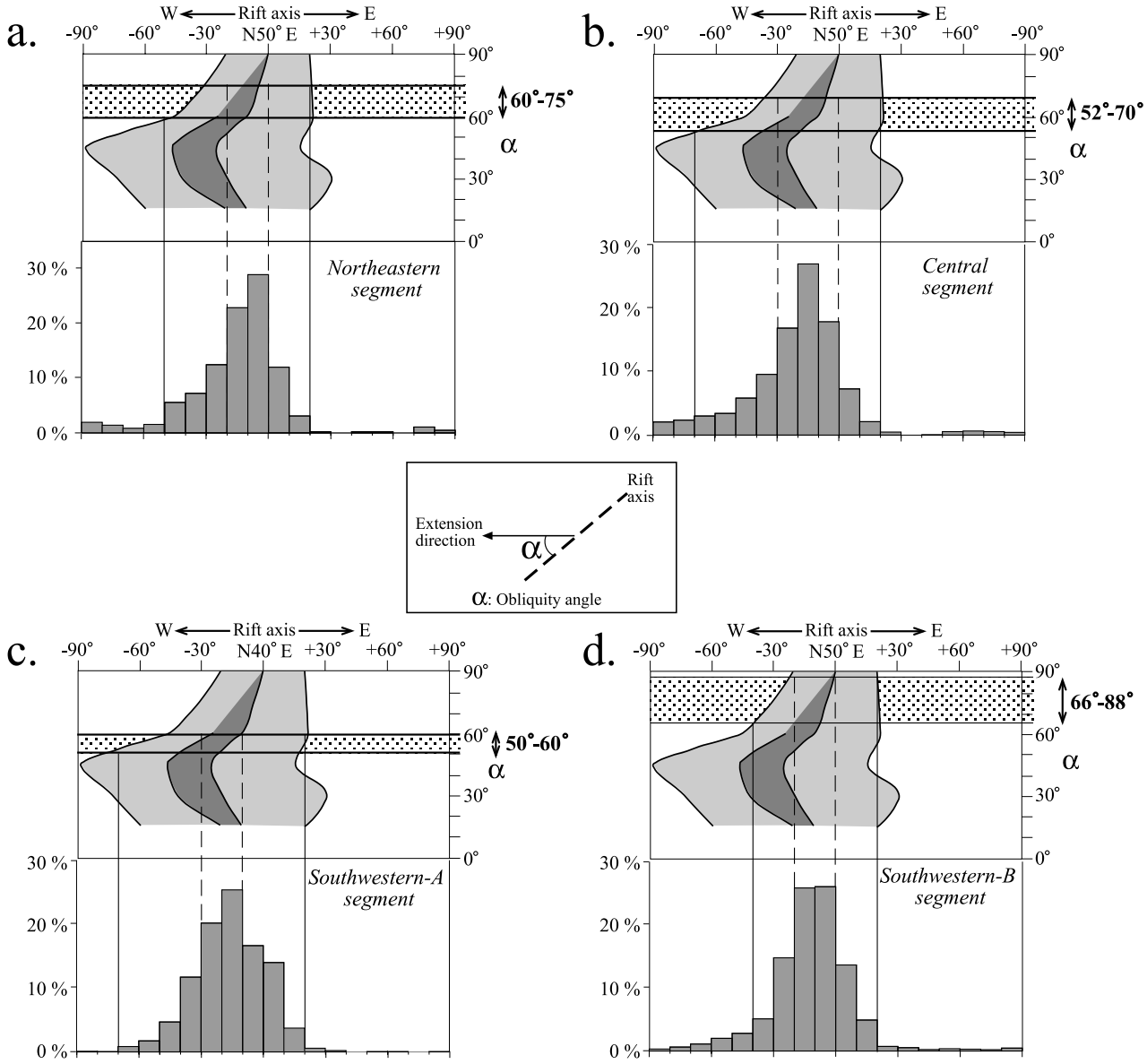

Figure 13. Estimation of the extension direction at the Tempe Rift from fault azimuthal distribution (histograms of fault azimuths; see Figure 9) by comparison with the experimental results of *Tron and Brun* [1991]. Experimental diagrams plot fault obliquity (*a*; explanation in the inset) against fault azimuth centered on the rift axis. Shaded areas represent the orientation span of experimental faults. The significant range of each histogram is adjusted to the light gray area of experimental data, with the main peak approximately coinciding with the dark gray area. (a) Northeastern segment. (b) Central segment. (c) Southwestern-A segment. (d) Southwestern-B segment.

arrangement. *Peacock and Sanderson* [1991] showed that the proximity of neighboring faults increases the displacement/length ratios determined for each individual segment. Most of the scatter observed in Figure 7 could be due to the fundamentally segmented nature of fault systems at the Tempe Rift. The large scale of the fault trace maps used by *Wilkins et al.* [2002] does not allow recognizing such detailed geometries, therefore reducing the influence of this scatter source. Apart from this, the more populated zones of the displacement/length diagrams for the Tempe Rift (density contours in Figure 7) show an acceptable agreement with the previous data from Tempe Terra [*Wilkins et al.*, 2002] and with the theoretical scaling relations calculated by *Schulz et al.* [2006] for Mars basaltic rock masses (thick dashed line in Figure 8). Comparison with data from terrestrial normal faults (Figure 8) suggests that displacement/length ratios for Martian normal faults are shifted to smaller values of displacement, apart from the scatter associated with fault geometry, which confirms the results of *Schultz et al.* [2006]. This feature is mainly a consequence of the distinct planetary gravities [*Schulz et al.*, 2006]. As a note of caution, it must be indicated that the

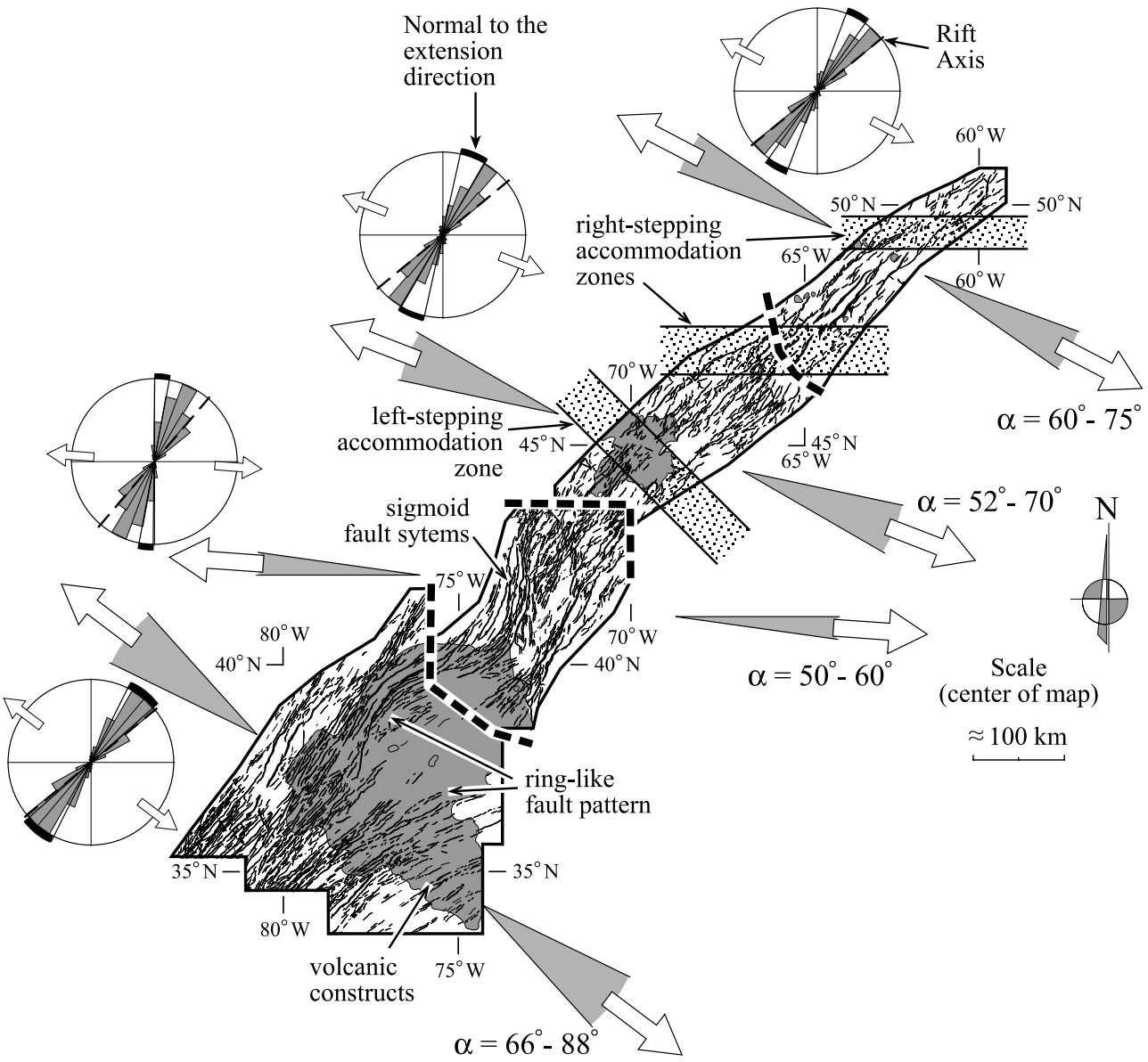

Figure 14. Tectonic sketch of Tempe Rift showing the fault map (Mercator projection), the estimated extension direction at each segment (including confidence intervals and polar diagrams with the location of the rift axis and the normal to the extension direction), and the location of some relevant structural and volcanic features, such as accommodation zones, sigmoid fault systems, and volcanic constructs. The estimation of the obliquity angle (α) is represented in Figure 13.

displacement/length ratio seems to be affected by isostatic forces on Earth, which can largely modify and even destroy the correlation between displacement and length for normal faults tens of kilometers long [*Cowie and Scholz*, 1992]. Most of the faults measured at the Tempe Rift are more than 10 km long (Figure 7) and therefore it has not been possible to compare terrestrial and Martian normal faults spanning the same length intervals. Future high-resolution images of Mars should be used to obtain detailed displacement/length ratios of small normal faults, with lengths shorter than a few kilometers. Comparison with large terrestrial strike-slip and thrust faults that do not show the isostatic influence also reveals the smaller displacement/length ratio of the Martian faults (Figure 8).

[31] Analog experiments [*Clifton et al.*, 2000; *Ackermann et al.*, 2001] have shown that fault scaling relationships depend on three main parameters: the obliquity angle (α), the deformation intensity, and the thickness of the mechanical layer (t_m). The mechanical layer represents the rock body containing the faults and, for regional-scale studies its thickness is comparable to the seismogenic thickness [*Scholz and Contreras*, 1998]. Experimental results indicate that the average fault spacing, the fractal dimension, and the average and maximum fault lengths increase with α [*Clifton*

et al., 2000]. In turn, the average and maximum observed fault lengths, sum of fault lengths, regularity of fault spacing, and fractal dimension increase with extension, while fault spacing decreases with extension [*Ackermann et al.*, 2001]. The fractal dimension also increases with t_m, but the length parameters and the average spacing decrease with t_m [*Ackermann et al.*, 2001].

[32] It is not easy to interpret the data on Table 1 according to these experimental results. The available data do not suggest a significant change of strain values along the Tempe Rift [*Hauber and Kronberg*, 2001]. However, new detailed, segment-by-segment determinations are necessary. The southwestern-A segment, probably rifted under the lowest α angle, shows the largest length parameters and fractal dimension. This is contrary to what it is expected from the experimental data unless high extension or low t_m values overwhelmed the effects of α. The small fault spacing at the southwestern-B segment can only be explained with a high extension value and/or high t_m. Therefore it is here believed that data of Tempe Terra are reflecting a complex interplay between the deformation intensity, α and t_m, with the crustal thickness playing the dominant role through a net increase in t_m from northeast to southwest along the rift. A thicker mechanical crust at the southwest of Tempe Rift could explain the more distributed fault pattern (see *Schlische et al.* [2002] for a definition of distributed normal faulting) and the greater width of the rift zone there. An increase in crustal thickness from Tempe Fossae toward the center of Tharsis [*Banerdt and Golombek*, 2000] agrees with these observations.

[33] Although fit to power law functions cannot be completely excluded on statistical grounds for segments northeastern and southwestern-A, the fault-length distributions of Tempe Rift are best described by exponential functions. This is similar to the results obtained at mid-ocean ridges on Earth [e.g., *Cowie*, 1998]. Exponential fault-length distributions have been explained due to either small width of the active zone or small thickness of the brittle crust that generates non-interacting faults spanning the mechanical layer [*Cowie*, 1998]. A number of independent criteria suggest localized deformation and weakly interacting faults at Tempe Rift, including the low values of the fractal dimension ($D < 2$) and the non-randomness of fault centroids, apart from the observed exponential cumulative size-frequency distribution of fault lengths. *Wilkins and Schultz* [2000] already considered the graben at Tempe Terra as not kinematically coherent (weakly interacting) based on the observed displacement deficit for fault arrays.

[34] Non-random and exponential fault populations are characteristics of the saturation stage of rift evolution described by *Ackermann et al.* [2001]. Large extension values are normally needed in the analog experiments to attain this mature stage. This contrasts with the low to moderate stretching estimated for Tempe Fossae by *Hauber and Kronberg* [2001]. Three explanations can be advanced to explain this apparent paradox. First, low values of thickness of the mechanical layer have been deduced at Tempe Rift in this work, which rends it more akin from a mechanical and structural point of view to the terrestrial oceanic crust. Second, the work of *Schultz et al.* [2006] shows that faults and fault systems of Mars must necessarily show smaller displacements than on Earth, due to differences in the planetary gravities. And third, the displacement component parallel to the rift axis has not yet been determined. It can be predicted that this component should moderately increase the estimated deformation value in at least the southwestern-A segment.

[35] Scaled experimental models allow us to analyze the inception and temporal evolution of deformation, and not only the final deformation state observed in Nature. Models are also used to simulate structural systems under different boundary conditions. Therefore they cast light on and give support to real world studies. Benefits of this comparison between experimental models and natural examples are particularly clear in the interpretation of terrestrial rift systems [e.g., *Clifton et al.*, 2000; *McClay et al.*, 2001; *Schlische et al.*, 2002]. Although this work shows a successful application of the results of models of oblique rifting to the Tempe Rift, these models are in fact scaled according to terrestrial parameters. Further analog experiments are needed to simulate orthogonal and oblique extension of the Martian crust, that accurately reflect the gravity, crustal thickness and mechanical properties of Mars.

5.3. Tectonic Implications of the Oblique Rifting at the Tempe Rift

[36] The Tempe Rift is a part of a complex group of extensional structures that radiate outward from Tharsis [e.g., *Plescia and Saunders*, 1982]. The tectonic history of the Tempe Rift is intimately related to that of Tharsis, as shown by the NE-trending alignment of the Tempe Rift with the Tharsis Montes [*Hauber and Kronberg*, 2001]. Interestingly, the Tharsis Montes are a consequence of an Amazonian tectono-magmatic episode [e.g., *Anderson et al.*, 2001], considerably younger than the main event of oblique rifting at Tempe (>3.5 Gy). This attests the long-lived tectonic activity of some crustal-scale accidents that crosscut the entire Tharsis region, like the Tharsis Montes-Tempe Rift weakness zone (TTWZ). The analysis of the successive tectonic episodes that affected Tharsis [*Plescia and Saunders*, 1982; *Anderson et al.*, 2001] clearly shows complex time-evolving stress fields [*Mège and Masson*, 1996b] and changing locations of the estimated centers of radial structures [*Anderson et al.*, 2001]. Large old structures such as the TTWZ could have been reactivated during each new tectonic episode. Apart from rheological and mechanical factors, the relative orientation of previous structures with respect to the principal stress trajectories of the successive stress fields determines whether these structures can be potentially reactivated and, if that were the case, what would the kinematic pattern (orthogonal or oblique rifting, strike-slip displacement) be. Reactivation of the northern part of the TTWZ as a sinistral oblique rift occurred late in the Noachian. Similar detailed analyses of other zones surrounding Tharsis are necessary before a complete picture of this episode could be presented.

[37] As for Martian tectonic evolution, these results could indicate that mechanical models based exclusively on simple stress fields are insufficient to explain in detail Tharsis faults' architecture. It is increasingly clear that in order to reconstruct the history of a tectono-magmatic province more than 5,000 km wide we will need to piece together complex and evolving stress fields. Moreover, if *Anguita et al.* [2006] are right in their assumption of Earth-size mountain chains

in Hesperian Mars, then huge tangential stresses are surely inescapable, and every revision of the geometry of Tharsis fractures could add to a new Martian tectonic landscape.

6. Conclusions

[38] A detailed analysis of the fault populations observed at the Tempe Rift on Mars shows that this extensional region was probably generated under oblique rifting, with a component of sinistral displacement. Values of the angle (α) between the extension direction and the rift axis vary from a minimum of 50° (southwestern-A segment) to a maximum of 88° (southwestern-B segment). By comparison with well-known terrestrial examples, structural inheritance and a long Noachian tectonic activity with time-changing deformation fields can explain this period of oblique extension. Observation of exponential fault length-frequency distributions of fault populations suggests that faults were weakly interacting at Tempe Rift. This fault scaling relationship makes the Noachian crust at Tempe more comparable to the oceanic than to the continental crust of our planet. Results of the fractal analysis of fault trace maps, with fractal dimension lower than 2, and the non-random spatial distribution of fault centroids are evidences of localized, inhomogeneous deformation. Most fault scaling relationships indicate that the thickness of the faulted mechanical layer was small and that it increased toward the southwest (i.e., toward Tharsis center), although the influence of deformation intensity, poorly constrained by now, must be taken into account.

[39] Fault crosscutting relationships observed at Mars should be revisited following the guidelines provided by the increasing amount of information available from oblique-extension tectonic scenarios. Although the available physical experiments are useful to interpret fault patterns at Mars, new models should be designed with the proper scaling relations. This could surely contribute to improve our understanding of the tectonic significance and evolution of intricate Noachian fault sets. It can be anticipated that a more rigorous, complex, lively and interesting tectonic description of the entire Tharsis region would emerge from these studies.

[40] **Acknowledgments.** The authors would like to thank Ernst Hauber and Robert C. Anderson for a thorough and useful review. We thank the Viking and Mars Global Surveyor teams for the use of Viking context images. C.F. acknowledges financial support from Spanish Ministry of Education and Science project CGL2004-06808-CO4-02.

References

Ackermann, R. V., R. W. Schlische, and M. O. Withjack (2001), The geometric and statistical evolution of normal fault systems: An experimental study of the effects of mechanical layer thickness on scaling laws, *J. Struct. Geol.*, *23*, 1803–1819.

Anderson, R. C., A. F. C. Haldemann, J. M. Dohm, M. P. Golombek, B. J. Franklin, and J. Lias (1999), Significant centers of tectonic activity as identified by wrinkle ridges for the western hemisphere of Mars, *Lunar Planet. Sci.*, *XXX*, Abstract 1972.

Anderson, R. C., J. M. Dohm, M. P. Golombek, A. F. Haldemann, B. J. Franklin, K. L. Tanaka, J. Lias, and B. Peer (2001), Primary centers and secondary concentrations of tectonic activity through time in the western hemisphere of Mars, *J. Geophys. Res.*, *106*, 20,563–20,585.

Anguita, F., A. F. Farelo, V. López, C. Mas, M. J. Muñoz, A. Márquez, and J. Ruiz (2001), Tharsis dome, Mars: New evidence for Noachian-Hesperian thick-skin and Amazonian thin-skin tectonics, *J. Geophys. Res.*, *106*, 7577–7589.

Anguita, F., C. Fernández, G. Cordero, S. Carrasquilla, J. Anguita, A. Núñez, S. Rodríguez, and J. García (2006), Evidences for a Noachian-Hesperian orogeny in Mars, *Icarus*, *185*(2), 331–357.

Banerdt, W. B., and M. P. Golombek (2000), Tectonics of the Tharsis region of Mars: Insights from MGS topography and gravity, *Lunar Planet. Sci.*, *XXXI*, Abstract 2038.

Bonini, M., T. Souriot, M. Boccaletti, and J. P. Brun (1997), Successive orthogonal and oblique extension episodes in a rift zone: Laboratory experiments with application to the Ethiopian Rift, *Tectonics*, *16*, 347–362.

Borraccini, F., L. Lanci, F. C. Wezel, and D. Baioni (2005), Crustal extension in the Ceraunius Fossae, Northern Tharsis Region, Mars, *J. Geophys. Res.*, *110*, E06006, doi:10.1029/2004JE002373.

Cailleau, B., T. R. Walter, P. Janle, and E. Hauber (2003), Modeling volcanic deformation in a regional stress field: Implications for the formation of graben structures on Alba Patera, Mars, *J. Geophys. Res.*, *108*(E12), 5141, doi:10.1029/2003JE002135.

Carr, M. H. (1974), Tectonism and volcanism of the Tharsis region of Mars, *J. Geophys. Res.*, *79*, 3943–3949.

Clifton, A. E., and R. W. Schlische (2001), Nucleation, growth, and linkage of faults in oblique rift zones: Results from experimental clay models and implications for maximum fault size, *Geology*, *29*, 455–458.

Clifton, A. E., and R. W. Schlische (2003), Fracture populations on the Reykjanes Peninsula, Iceland: Comparison with experimental clay models of oblique rifting, *J. Geophys. Res.*, *108*(B2), 2074, doi:10.1029/2001JB000635.

Clifton, A. E., R. W. Schlische, M. O. Withjack, and R. V. Ackermann (2000), Influence of rift obliquity on fault-population systematics: Results of experimental clay models, *J. Struct. Geol.*, *22*, 1491–1509.

Cowie, P. A. (1998), Normal fault growth in three dimensions in continental and oceanic crust, in *Faulting and Magmatism at Mid-Ocean Ridges*, *Geophys. Monogr. Ser.*, vol. 106, edited by W. R. Buck et al., pp. 325–348, AGU, Washington, D. C.

Cowie, P. A., and C. H. Scholz (1992), Displacement-length scaling relationship for faults: Data synthesis and discussion, *J. Struct. Geol.*, *14*, 1149–1156.

Cressie, N. A. C. (1993), *Statistics for Spatial Data*, 900 pp., John Wiley, New York.

Dauteuil, O., P. Huchon, F. Quemeneur, and T. Souriot (2001), Propagation of an oblique spreading centre: The western Gulf of Aden, *Tectonophysics*, *332*, 423–442.

Ferrill, D. A., D. Y. Wyrick, A. P. Morris, D. W. Sims, and N. M. Franklin (2004), Dilational fault slip and pit chain formation on Mars, *GSA Today*, *14*(10), 4–12, doi:10.1130/1052-5173(2004)014<4:DFSAPC>2.0.CO;2.

Forsythe, R. D., and J. R. Zimbelman (1988), Is the Gordii Dorsum escarpment on Mars an exhumed transcurrent fault?, *Nature*, *336*, 143–146.

Golombek, M. P., K. L. Tanaka, and B. J. Franklin (1996), Extension across Tempe Terra, Mars, from measurements of fault scarp widths and deformed craters, *J. Geophys. Res.*, *101*, 26,119–26,130.

Hauber, E., and P. Kronberg (1999), Differences in style and age of extensional faulting: Examples from the Northern Tharsis Province, Mars, *Lunar Planet. Sci.*, *XXX*, Abstract 1568.

Hauber, E., and P. Kronberg (2001), Tempe Fossae, Mars: A planetary analogon to a terrestrial continental rift?, *J. Geophys. Res.*, *106*, 20,587–20,602.

Hauber, E., and P. Kronberg (2005), The large Thaumasia graben on Mars: Is it a rift?, *J. Geophys. Res.*, *110*, E07003, doi:10.1029/2005JE002407.

Keep, M., and K. R. McClay (1997), Analogue modeling of multiphase rift systems, *Tectonophysics*, *273*, 239–270.

Mangold, N., P. Allemand, P. G. Thomas, and G. Vidal (2000), Chronology of compressional deformation on Mars: Evidence for a single and global origin, *Planet. Space Sci.*, *48*, 1201–1211.

McClay, K. R., T. Dooley, R. Gloaghen, P. Whitehouse, and S. Khalil (2001), Analogue modeling of extensional fault architectures: Comparisons with natural rift fault systems, paper presented at PESA Eastern Australian Basins Symposium, Pet. Explor. Soc. of Aust., Melbourne, Victoria, Australia.

McClay, K. R., T. Dooley, P. Whitehouse, and M. Mills (2002), 4-D evolution of rift systems: Insights from scales physical models, *AAPG Bull.*, *86*, 935–959.

Mège, D., and P. Masson (1996a), Stress models for Tharsis formation, Mars, *Planet. Space Sci.*, *44*, 1471–1497.

Mège, D., and P. Masson (1996b), A plume tectonics model for the Tharsis province, Mars, *Planet. Space Sci.*, *44*, 1499–1546.

Melosh, H. J. (1980), Tectonic patterns on a reoriented planet: Mars, *Icarus*, *44*, 745–751.

Mueller, K., and M. Golombek (2004), Compressional structures on Mars, *Annu. Rev. Earth Planet. Sci.*, *32*, 435–464.

Peacock, D. C. P., and D. J. Sanderson (1991), Displacement and segment linkage in relay ramps in normal fault zones, *J. Struct. Geol.*, *13*, 721–733.

Plescia, J. B., and R. S. Saunders (1982), Tectonic history of the Tharsis region, Mars, *J. Geophys. Res.*, *87*, 9775–9791.

Robin, P. Y. F., and E. C. Jowett (1986), Computerized density contouring and statistical evaluation of orientation data using counting circles and continuous weighting functions, *Tectonophysics*, *121*, 207–223.

Schlische, R. W., S. S. Young, R. V. Ackermann, and A. Gupta (1996), Geometry and scaling relations of a population of very small rift related normal faults, *Geology*, *24*, 683–686.

Schlische, R. W., M. O. Withjack, and G. Eisenstadt (2002), An experimental study of the secondary deformation produced by oblique-slip normal faulting, *AAPG Bull.*, *86*, 885–906.

Scholz, C. H., and J. C. Contreras (1998), Mechanics of continental rift architecture, *Geology*, *26*, 967–970.

Schultz, R. A. (1989), Strike-slip faulting of ridged plains near Valles Marineris, *Mars, Nature*, *341*, 424–426.

Schultz, R. A., and A. N. Fori (1996), Fault-length statistics and implications of graben sets at Candor Mensa, Mars, *J. Struct. Geol.*, *18*, 373–383.

Schultz, R. A., and K. L. Tanaka (1994), Lithospheric-scale buckling and thrust structures on Mars: The Coprates rise and south Tharsis ridge belt, *J. Geophys. Res.*, *99*, 8371–8385.

Schultz, R. A., C. H. Okubo, and S. J. Wilkins (2006), Displacement-length scaling relations for faults on the terrestrial planets, *J. Struct. Geol.*, *28*, 2182–2193, doi:10.1016/j.jsg.2006.03.034.

Scott, D. H., and J. M. Dohm (1990), Chronology and global distribution of fault and ridge systems on Mars, *Lunar Planet. Sci.*, *20*, 487–501.

Scott, D. H., and K. L. Tanaka (1986), Geological map of the western equatorial region of Mars, *U.S. Geol. Surv. Misc. Invest. Ser.*, *Map I-1802–A*, scale 1:15M.

Swan, A. R. H., and M. Sandilands (1995), *Introduction to Geological Data Analysis*, 446 pp., Blackwell Sci., Oxford, U. K.

Tanaka, K. L., M. P. Golombek, and W. B. Banerdt (1991), Reconciliation of stress and structural stories of the Tharsis region of Mars, *J. Geophys. Res.*, *96*, 15,617–15,633.

Tron, V., and J. P. Brun (1991), Experiments on oblique rifting in brittle-ductile systems, *Tectonophysics*, *188*, 71–84.

Vignes-Adler, M., A. Le Page, and P. M. Adler (1991), Fractal analysis of fracturing in two African regions, from satellite imagery to ground scale, *Tectonophysics*, *196*, 69–86.

Walsh, J. J., and J. Watterson (1993), Fractal analysis of fracture patterns using the standard box-counting technique: Valid and invalid methodologies, *J. Struct. Geol.*, *15*, 1509–1512.

Watters, T. R. (1991), Origin of periodically spaced wrinkle ridges on the Tharsis Plateau of Mars, *J. Geophys. Res.*, *96*, 15,599–15,616.

Watters, T. R. (1993), Compressional tectonism on Mars, *J. Geophys. Res.*, *98*, 17,049–17,060.

Watters, T. R., and D. M. Janes (1995), Coronae on Venus and Mars: Implications for similar structures on Earth, *Geology*, *23*, 200–204.

Watters, T. R., and T. A. Maxwell (1983), Crosscutting relations and relative ages of ridges and faults in the Tharsis region of Mars, *Icarus*, *56*, 278–298.

Watters, T. R., and T. A. Maxwell (1986), Orientation, relative age, and extent of the Tharsis Plateau ridge system, *J. Geophys. Res.*, *91*, 8113–8125.

Whithjack, M. O., and W. R. Jamison (1986), Deformation produced by oblique rifting, *Tectonophysics*, *126*, 99–124.

Wilkins, S. J., and R. A. Schultz (2000), Displacement-length relationships of grabens in Tempe Terra, Mars, *Eos Trans. AGU*, *81*(48), Fall Meet. Suppl., Abstract T21B-04.

Wilkins, S. J., and R. A. Schultz (2003), Cross faults in extensional settings: Stress triggering, displacement localization, and implications for the origin of blunt troughs at Valles Marineris, Mars, *J. Geophys. Res.*, *108*(E6), 5056, doi:10.1029/2002JE001968.

Wilkins, S. J., R. A. Schultz, R. C. Anderson, J. M. Dohm, and N. H. Dawers (2002), Deformation rates from faulting at the Tempe Terra extensional province, Mars, *Geophys. Res. Lett.*, *29*(18), 1884, doi:10.1029/2002GL015391.

Wise, D. U., M. P. Golombek, and G. E. McGill (1979), Tharsis province of Mars: Geologic sequence, geometry, and a deformation mechanism, *Icarus*, *38*, 456–472.

F. Anguita, Departamento de Petrología y Geoquímica, Universidad Complutense de Madrid, E-28071 Madrid, Spain.

C. Fernández, Departamento de Geodinámica y Paleontología, Universidad de Huelva, E-21071 Huelva, Spain. (fcarlos@uhu.es)